National Library
of Canada

Acquisitions and
Bibliographic Services Branch

395 Wellington Street
Ottawa, Ontario
K1A 0N4

Bibliothèque nationale
du Canada

Direction des acquisitions et
des services bibliographiques

395, rue Wellington
Ottawa (Ontario)
K1A 0N4

Your file Votre référence

Our file Notre référence

NOTICE

The quality of this microform is heavily dependent upon the quality of the original thesis submitted for microfilming. Every effort has been made to ensure the highest quality of reproduction possible.

If pages are missing, contact the university which granted the degree.

Some pages may have indistinct print especially if the original pages were typed with a poor typewriter ribbon or if the university sent us an inferior photocopy.

Reproduction in full or in part of this microform is governed by the Canadian Copyright Act, R.S.C. 1970, c. C-30, and subsequent amendments.

AVIS

La qualité de cette microforme dépend grandement de la qualité de la thèse soumise au microfilmage. Nous avons tout fait pour assurer une qualité supérieure de reproduction.

S'il manque des pages, veuillez communiquer avec l'université qui a conféré le grade.

La qualité d'impression de certaines pages peut laisser à désirer, surtout si les pages originales ont été dactylographiées à l'aide d'un ruban usé ou si l'université nous a fait parvenir une photocopie de qualité inférieure.

La reproduction, même partielle, de cette microforme est soumise à la Loi canadienne sur le droit d'auteur, SRC 1970, c. C-30, et ses amendements subséquents.

Canada

University of Alberta

A Reprojection Method for Performing Attenuation Correction in SPECT Imaging

by

Eugene Mah ©

A thesis submitted to the Faculty of Graduate Studies and Research in partial fulfillment of the requirements for the degree of Master of Science

Department of Radiology and Diagnostic Imaging

Edmonton, Alberta

Spring 1996

National Library
of Canada

Acquisitions and
Bibliographic Services Branch

395 Wellington Street
Ottawa, Ontario
K1A 0N4

Bibliothèque nationale
du Canada

Direction des acquisitions et
des services bibliographiques

395, rue Wellington
Ottawa (Ontario)
K1A 0N4

Your file Votre référence

Our file Notre référence

The author has granted an irrevocable non-exclusive licence allowing the National Library of Canada to reproduce, loan, distribute or sell copies of his/her thesis by any means and in any form or format, making this thesis available to interested persons.

L'auteur a accordé une licence irrévocable et non exclusive permettant à la Bibliothèque nationale du Canada de reproduire, prêter, distribuer ou vendre des copies de sa thèse de quelque manière et sous quelque forme que ce soit pour mettre des exemplaires de cette thèse à la disposition des personnes intéressées.

The author retains ownership of the copyright in his/her thesis. Neither the thesis nor substantial extracts from it may be printed or otherwise reproduced without his/her permission.

L'auteur conserve la propriété du droit d'auteur qui protège sa thèse. Ni la thèse ni des extraits substantiels de celle-ci ne doivent être imprimés ou autrement reproduits sans son autorisation.

ISBN 0-612-10734-5

Canada

University of Alberta

Library Release Form

Name of Author: Eugene Mah

Title of Thesis: A Reprojection Method for Performing Attenuation Correction in SPECT Imaging

Year this Degree Granted: 1996

Permission is hereby granted to the University of Alberta Library to reproduce single copies of this thesis and to lend or sell such copies for private, scholarly, or scientific research purposes only.

The author reserves all other publication and other rights in association with the copyright in the thesis, and except as hereinbefore provided, neither the thesis nor any substantial portion thereof may be printed or otherwise reproduced in any material or electronic form whatever without the author's prior written permission.

Eugene Mah

Eugene Mah
#10 14250 80 St
Edmonton, Alberta
T5C 1L6
November 8, 1995

University of Alberta

Faculty of Graduate Studies and Research

The undersigned certify that they have read, and recommend to the Faculty of Graduate Studies and Research for acceptance, a thesis entitled *A Reprojection Method for Performing Attenuation Correction in SPECT Imaging* submitted by Eugene Mah in partial fulfillment of the requirements for the degree of Master of Science

Supervisor: Larry J. Filipow, D. Phil.

Committee member: Stuart Jackson, Ph.D.

Committee member: Rick Hooper, Ph.D.

Committee member: Conor Maguire, M.D.

Committee member: Alexander J. B. McEwan, M.B.B.S.

November 14, 1995

“For I am a Bear of Very Little Brain, and long words Bother me”

Winnie-The-Pooh, A. A. Milne

Abstract

One of the major factors affecting quantitative SPECT is the problem of photon attenuation. It is well known that approximately 50% of the photons emitted from Tc-99m (140 keV) will be absorbed by about 5 cm of water. Because of this, several methods have been developed to correct SPECT images for photon attenuation. Many methods currently being investigated are iterative methods which are computationally intensive and require many iterations to produce a solution. In this work, a method is developed based on using reconstructed images to estimate the contribution of each source voxel to the raw projection data. Each pixel in the image is reprojected and weighted with an exponential attenuation length $exp\,(\int \mu\,(x, y)\,dy)$ evaluated from the pixel to the detector. The weighting factor is determined from an attenuation map obtained using a transmission scan which is acquired simultaneously with the emission scan. The research presented here will investigate the potential usefulness of the attenuation correction method developed using several phantom studies.

Acknowledgments

I'd like to thank the following people for all their help without which most of this project would not have been possible,

My family,

Larry J. Filipow, D. Phil, for all of his support on this project,

Suzanne, for her invaluable friendship,

Rick, Tom, Joe and Mike, for making sure I had fun and didn't take anything too seriously,

the staff in the Nuclear Medicine for putting up with me while I tried not to break anything too severely,

the Department of Radiology, for their support and letting me play with all the toys,

and Yaenette, for putting up with all of this.

Table of Contents

CHAPTER 1

Nuclear Medicine Imaging Principles 1-1

Introduction to SPECT 1-1
Gamma Camera 1-3
SPECT Imaging Principles 1-6
Photon Attenuation 1-9
Effects of Attenuation and Scatter 1-12

CHAPTER 2

Attenuation Correction Algorithms 2-16

Exponential Radon Transform 2-16
Pre-reconstruction Correction 2-19
Postprocessing Correction 2-20
Intrinsic Correction 2-21
  Iterative Algorithms 2-23
Non-uniform Attenuation Correction 2-24
  Transmission SPECT Isotopes 2-25
  Transmission Source Geometries 2-28
Scatter Correction 2-34

CHAPTER 3 Reprojection Correction Algorithm 3-37

- Rationale 3-37
- Derivation 3-39

CHAPTER 4 Materials and Methods 4-44

- Picker PRISM 3000 SPECT system 4-44
- Line Source/Holder Assembly 4-45
- Phantoms 4-47
  - Linearity Phantom 4-47
  - Uniformity Phantom 4-48
  - Resolution Phantom 4-49
  - Brain Phantom 4-50
  - Grid Phantom 4-50
- Acquisition Protocols 4-52
- Attenuation Correction Algorithms 4-59
  - Reprojection algorithm 4-59
  - Chang algorithm 4-60

CHAPTER 5 Results and Discussion 5-63

- Attenuation Map 5-63
  - Linearity 5-63
  - Resolution 5-67
- Digital Simulations 5-68
- SPECT Sensitivity 5-72
- Uniform Water Phantom 5-76
- Brain Phantom 5-86
  - Brain Phantom Quantitation 5-96
- Grid Phantom 5-98

CHAPTER 6 Further Work 6-108

Further Work 6-108

CHAPTER 7 Conclusion 7-112

Conclusion 7-112

CHAPTER 8 Appendix A: Program listings A-115

- Transmission scan conversion program A-115
  - Transmission/emission data subtraction A-115
  - Transmission to m conversion A-116
- Fan beam projection algorithm A-117
  - Ray tracing algorithm A-117
  - Fan beam projection routine A-119
- Non-uniform Chang algorithm A-122

CHAPTER 9 Bibliography B-126

List of Figures

Photon attenuation $N = N_o e^{-\Sigma \mu_i x}$ 1-9

Compton scattering process 1-10

Different types of Compton scatter events: A) detected multiple scatter events B) unscattered photopeak events C) small angle scattered event D) undetected multiple scatter events 1-11

Photoelectric effect 1-12

Reconstructed SPECT slice of a uniform water phantom 1-13

Profile through the center of the image in Figure 5. The center of the phantom is pixel 64. 1-14

Geometry for the attenuated Radon transform. 2-18

Flood source - parallel hole collimator geometry 2-29

Scanning line source - parallel hole collimator geometry 2-30

Point source - cone beam geometry 2-32

Line source - fan beam collimator geometry 2-33

Attenuated Radon transform projection geometry 3-40

Pixel intersection length for one pixel 3-41

Picker PRISM 3000 SPECT gantry 4-44

a) Data Spectrum line source
b) Line source/holder assembly mounted on the SPECT gantry 4-46

Schematic of the line source setup. 4-47

Cross section of inserts in the linearity phantom: 1) simulated bone 2) low density plastic 3) Perspex 4) medium density plastic 5) acrylic 6) water 7) high density plastic 8) aluminum 4-48

Uniform water cylinder 4-48

Jaszczak phantom 4-49

Grid phantom 4-51

Simulated attenuation map of the grid phantom with 4 blocks of aluminum. 4-52

Projection preprocessing steps to remove emission data from the combined emission/transmission data in head 1 4-54

Grid phantom configurations: Dark gray - water filled inserts. Light grey - sources. Black - aluminum blocks. A) No aluminum blocks, B) 2 2x1 aluminum blocks C) 4 2x1 aluminum blocks 4-58

Transmission images of the linearity phantom. Left) through the phantom base. Right) through the water bag. 5-65

Plot of linear attenuation coefficients vs. reconstructed pixel value. Points are the ROI data. The solid line represents Equation 28 5-67

Attenuation map of the rods in the Jaszczak phantom. 5-68

Simulated SPECT data for the grid phantom. 5-69

Attenuation correction of simulated SPECT images. 5-70

Line profiles through the simulated source at the center of the phantom. Counts normalized to 1. 5-72

Relationship between source activity concentration and pixel counts/second. 5-75

Reconstructed slice from a SPECT study. 5-76

Line profile through the center of Figure 31. 5-77

Attenuation map of the uniform water phantom. 5-77

Line profile through the center of Figure 33. 5-78

Side view of line source-detector arrangement showing inter-slice crosstalk events. 5-79

Attenuation corrected SPECT image of Figure 31 using the reprojection method. 5-81

Line profile through the center of Figure 36. 5-82

Attenuation correction of the uniform water phantom using the Chang method. 5-83

Line profile through the center of Figure 38. 5-84

Quantitative analysis of the water phantom. 5-85

Reconstructed SPECT slices from the brain phantom. 5-87

Attenuation maps of the brain phantom. 5-88

Reprojection corrected brain phantom images. 5-89

Chang corrected brain phantom images. 5-90

Slice 9 from the original SPECT, reprojection and Chang corrected images. 5-91

Attenuation map for Figure 45. 5-92

Line profile through the frontal lobe inserts of Figure 45. 5-93

Slice 14 of the brain phantom 5-94

Attenuation map corresponding to the SPECT slices in Figure 48. 5-95

Line profile through the frontal lobe inserts in Figure 48. 5-96

Quantitative analysis of the brain phantom. 5-96

SPECT slices through the middle of the grid phantom. 5-98

Line profiles through the central source of the grid phantom with 0, 2 and 4 aluminum inserts. 5-99

Attenuation map with no aluminum blocks. 5-99

Simulated attenuation map showing 4 aluminum inserts. 5-101

Reprojection corrected images. 5-102

Line profile through the central source in Figure 56. 5-103

Chang attenuation corrected images. 5-103

Line profiles through the central source of Figure 58. 5-104

Quantitative analysis of central source with no aluminum. 5-105

Quantitative analysis of outer source with no aluminum. 5-105

Quantitative analysis of central source with 4 aluminum blocks. 5-105

Quantitative analysis of outer source with 4 aluminum blocks. 5-106

List of Tables

Brain phantom insert activity 4-50

Narrow beam attenuation coefficients for the linearity phantom inserts 4-53

Attenuation coefficients for linearity phantom objects 5-64

ROI data from the linearity phantom. 5-66

SPECT sensitivity source concentrations. 5-73

ROI counts 5-74

CHAPTER 1

Nuclear Medicine Imaging Principles

1.1 Introduction to SPECT

The primary goal of nuclear medicine imaging is to obtain information about organ function rather than organ anatomy as with other diagnostic imaging modalities. To accomplish this, a pharmaceutical is labelled with a gamma ray emitting radioisotope (commonly Tc-99m) and injected into the body. The pharmaceutical is generally designed to target a specific organ, so that maximum uptake of the pharmaceutical occurs in the target organ (e.g. brain, liver, heart, kidney). The distribution of radiopharmaceutical uptake in various areas of the target organ can be used to indicate the presence of disease or abnormal function. In order to make this diagnosis though, a method of imaging the distribution of the radiopharmaceutical in the target organ is needed.

Planar images collected by a gamma camera serve to show the uptake of a tracer within a specific organ in the body. Lesions are indicated by abnormalities in the amount and uptake/clearance rates of the radiopharmaceutical, showing up as regions of increased or decreased activity relative to their surroundings.

One of the problems with planar imaging is that the images are a compression of three dimensional distributions onto two dimensional planes. Activity from above and below the target organ is blended into the same image, causing a decrease in the contrast and detectability of the lesion. This is especially noticeable for low contrast lesions, where the activity does not differ much from the surroundings.

One way around this problem is to use SPECT, Single Photon Emission Computed Tomography. SPECT provides a way of creating a 3D representation of the radiopharmaceutical distribution and displaying the distribution within the organ as a series of tomographic slices. SPECT images show a dramatic increase in contrast and detectability of lesions, because the background activity has been separated from the lesion itself.

Attenuation of the emitted gamma rays due to interactions within the body is a major problem in reconstructing SPECT images. Photon attenuation causes a significant loss in the number of photons detected from regions deep within the body and affects the ability to perform quantitative analysis on SPECT images. The result is decreased contrast in central regions and possible artifacts in the reconstructed images.

The objective of this thesis is to develop and investigate a simple, easy to implement method of correcting the reconstructed SPECT images for photon attenuation effects using an attenuation map obtained from a simultaneously acquired transmission computed tomography (TCT) scan. Projections from the SPECT acquisition are reconstructed and used to estimate the radiopharmaceutical distribution within the target organ. The SPECT slices are then reprojected using the attenuation map to correct the projections for attenuation.

1.2 Gamma Camera

To observe the radiopharmaceutical distribution within the target organ, a gamma camera (or Anger camera) is used. The gamma camera consists of a large single crystal of NaI(Tl) about 1 cm thick, an array of photomultiplier tubes (PMTs) and a computer. The NaI(Tl) crystal is the principle part of the gamma camera. It's purpose is to convert the gamma rays exiting the patient and interacting with the crystal to visible or ultraviolet light. A gamma ray photon travelling through the crystal interacts with the crystal lattice, depositing some or all of its energy within the crystal. The crystal scintillates, giving off a brief flash of light. The intensity of the flash is proportional to the amount of energy deposited within the crystal by the gamma ray.

Coupled to the NaI(Tl) crystal is an array of photomultiplier tubes (PMT) optically coupled to the crystal surface. Their purpose is to convert the scintillations into electrical signals, and amplify them. The PMT is made of a photocathode, which converts the scintillation photons into electrons, and a number of dynodes. A typical PMT usually has between 8-10 dynodes. Light incident on the photocathode causes electrons to be ejected via the photoelectric process. An electric field focuses these electrons to a series of dynodes. When the electrons hit the dynode, more electrons are released, and focused to the next dynode by a stronger electric field. In this manner, the PMT greatly amplifies the current pulse generated by the flash of light. The current pulse output by the PMT is directly proportional to the amount of light detected at the photocathode.

The resulting current pulse is then fed through a variety of preamplifiers and amplifiers. Pulses from the PMTs are processed by electronic circuitry to determine the location and energy of each scintillation event within the detector plane. Positioning circuitry generates X and Y pulses which specify the location of the scintillation event in the detector plane, while a summing circuit combines the pulses from the individual PMTs to produce a Z pulse which is proportional to the intensity of the scintillation and therefore the energy deposited within the crystal by the gamma ray producing the scintillation event. One or more single channel analyzers (SCA) processes the Z pulse to determine whether the scintillation event is to be accepted or rejected. Upper and lower level pulse height discriminators can be set so that only events within a certain energy range (Z pulse amplitude) are accepted. The position of the accepted pulses are collected by a computer and stored digitally to form an image.

In order to localize within the body each event detected by the crystal, a collimator is used, usually made of lead, tantalum or tungsten. The collimators play an important role in the formation of an image. The main purpose of the collimator is to restrict the direction from which the photons are detected. This helps to increase the resolution of the planar images, but reduces the sensitivity of the camera significantly. Only photons travelling toward the detector within the cone defined by the acceptance angle of the collimator holes (determined by the diameter and height of the collimator holes) are detected. The properties of the collimator, such as sensitivity (detection efficiency) and resolution, are determined by the shape, diameter and height of the collimator holes and the thickness of the collimator septa, all of which must be taken into consideration when designing collimators to optimize sensitivity and resolution. Septal thickness is chosen to minimize the penetration of photons crossing from one collimator hole into another (usually < 5% penetration). For low energy photons (140 keV) the septa thickness are typically less than 0.5 mm for lead. The shape, diameter and height of the collimator holes determine the resolution of the gamma camera system. Most collimators are designed with hexagonal holes to maximize the amount of detector used. The height (l) and diameter (d) of the collimator holes determine the acceptance angle of the collimator holes, thereby affecting resolution. For a point source a distance z above the camera, the full width-half maximum (FWHM) for a parallel hole collimator can be approximated by

$$R(z) \approx (l_e + z) \tan\alpha \qquad \text{(EQ 1)}$$

where l_e is the effective height of the collimator holes ($l_e < l$ in order to account for septal penetration) and α is the acceptance angle,

$$\tan\alpha = \frac{d}{l_e} \qquad \text{(EQ 2)}$$

As the height increases and diameter decreases, the acceptance angle of the collimator holes decreases and the collimator resolution increases. However, sensitivity decreases because more photons are rejected by the collimator. Designing collimators for a given energy range and imaging situation involves choosing the septal thickness and the collimator hole dimensions to optimize resolution and sensitivity.

Commonly used collimators are parallel hole, fan beam, cone beam, diverging and pin hole collimators. Each type of collimator is designed for a specific use. Parallel hole collimators consist of an array of holes perpendicular to the face of the crystal. The holes in fan beam collimators converge to a line parallel to the axis of rotation. Fan beam collimators offer increased sensitivity and are useful for imaging small organs since more of the crystal is used to image the radioisotope distribution. Cone beam collimators offer even greater sensitivity although they require a more complex orbit around the patient in order to acquire a complete data set for reconstruction.

1.3 SPECT Imaging Principles

SPECT works by acquiring a series of planar images of the radiopharmaceutical distribution at many different angles around the patient. The patient is placed on a table, and a single or multiple headed gamma camera mounted on a gantry rotates around the patient to acquire the projections. "Step and shoot" SPECT techniques are the most common, where the gantry moves the gamma camera head(s) to the next projection angle, stops, and acquires the data. Continuous rotation techniques also exist, where the gamma camera head(s) rotates continuously around the patient as the data is gathered. In both cases, the planar images are then reconstructed using a filtered backprojection reconstruction algorithm to reconstruct the radiopharmaceutical distribution.

Filtered backprojection is the most common method of reconstructing images because of its computational simplicity, and ease of hardware implementation. The backprojection process takes the projection data and projects it back across an image matrix. For each projection angle, the projection data are summed back across the projection rays onto the image matrix forming a representation of the object. Thus, each image pixel represents the summation of all the projection rays passing through it. With the simple backprojection process, the resulting image is artificially blurred. Mathematically, the reconstructed image is equivalent to convolving the true image with a 1/r blurring function, where r is a radial distance from a point. In practice, due to limited angular sampling, a star patter artifact is the result. To solve this problem, the filtered backprojection process was developed. In filtered backprojection, the spatial projections are transformed into frequency space using a Fourier transform and filtered with a ramp filter, which in frequency space increases linearly with spatial frequency up to a finite cut-off point. The purpose of the ramp filter is to compensate for the 1/r blurring that would otherwise occur with a straight backprojection operation [1]. The filtering is performed in the frequency domain, because there the operation is a simple multiplication of the transformed projection and the filter. An inverse Fourier transform is then applied to the filtered projections which are then backprojected. Mathematically, the filtered backprojection process looks like [1]

$$f_o(x, y) = \sum_{i=1}^{M}\sum_{j=1}^{N}\bar{p}(x_j;\theta_i)\,\delta(x_j - x\cos\theta_i + y\sin\theta_i) \qquad \text{(EQ 3)}$$

where M is the number of projection angles, N is the number of projection rays in each projection and $\bar{p}(x_j;\theta_i)$ is the projection $p(x_j;\theta_i)$ with the filter $h(x - x')$ applied,

$$\bar{p}(x;\theta_i) = \int p(x;\theta_i)\,h(x - x')\,dx' \qquad \text{(EQ 4)}$$

Details of the filtered backprojection process can be found in other sources [1,25,44,46]. Additional filters, such as a low pass filter, or Butterworth filters can be applied to reduce image noise. Adaptive resolution recovery filters such as the Metz or Wiener filters are also commonly used [2] to enhance the reconstructed images.

Recently, there has been significant work in other methods, such as maximum likelihood-expectation maximization (MLEM) algorithms [3, 15, 42, 47] which approach the reconstruction problem from a statistical viewpoint, and iterative filtered backprojection methods in which the projections are filtered, backprojected, projected and then compared with projections from the previous iteration [53, 58]. A method of incorporating attenuation/scatter correction and detector response functions is generally included in the projection and comparison steps. There has also been some work with using artificial neural networks (ANN) [4] in the reconstruction process. These methods are more computationally intensive, but are able to incorporate elements such as scatter, attenuation and detector response into the reconstruction process to produce a more accurate image of the radioisotope distribution.

1.4 Photon Attenuation

Photon attenuation for narrow beam geometry (which minimizes the number of scattered photons detected in the transmitted beam), consisting of both absorption and Compton scatter interactions, can be described by a simple equation $N = N_o e^{-\Sigma \mu_i x}$, where N_0 is the number of incident photons, and N is the number of photons emerging from a slab of material of thickness d with linear attenuation coefficient μ. This is illustrated in Figure 1. The linear attenuation coefficient depends on the type of material as well as the photon energy.

FIGURE 1 Photon attenuation $N = N_o e^{-\Sigma \mu_i x}$

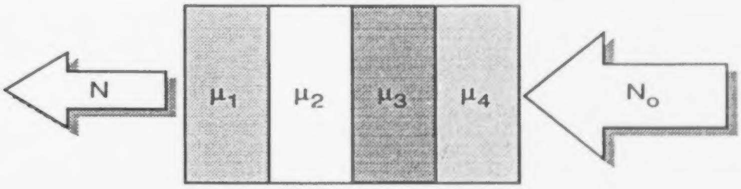

At 140 keV, the photon energies emitted by 99m-Tc, the most probable interaction a photon will experience is Compton scatter. The photon interacts with an electron in the outer shell of an atom (loosely bound) or an unbound electron, and is scattered an angle θ away from it's original direction of travel. The photon loses a small amount of energy that is transferred to an electron as illustrated in Figure 2 below.

FIGURE 2 Compton scattering process

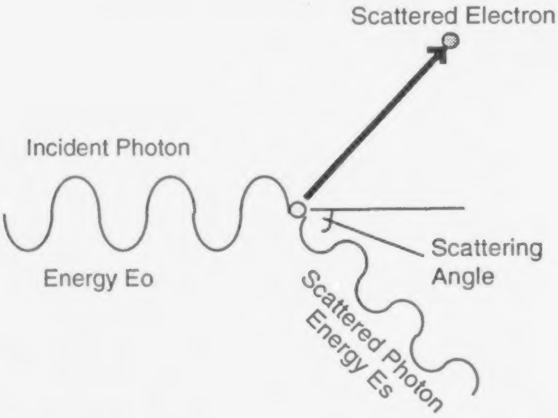

The energy of the scattered photon is related to the angle at which it is scattered at, and is given by the formula

$$E_s = \frac{E_o}{1 + \frac{E_o}{0.511}(1 - \cos\theta)} \qquad \text{(EQ 5)}$$

where E_0 and E_s are the energy of the incident and scattered photon in MeV and θ is the scattering angle. The larger the scattering angle, the greater the energy loss by the photon. The maximum energy loss occurs at a scattering angle of 180°. The photon will continue on through the material either eventually escaping from it or until it is absorbed, or scattering several more times until it is absorbed or escapes. If the photon escapes, and is detected by the gamma camera, it may be detected at a location far away from where it was emitted due to numerous scattering interactions. This is illustrated in Figure 3.

FIGURE 3

Different types of Compton scatter events: A) detected multiple scatter events B) unscattered photopeak events C) small angle scattered event D) undetected multiple scatter events

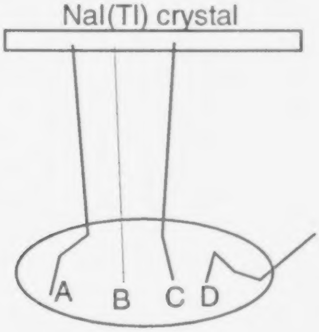

Absorption of photons occurs via the photoelectric effect (Figure 4). This occurs when a photon interacts with a tightly bound orbital electron. The photon is absorbed completely, and an electron is ejected with an energy equal to the difference between the photon energy and the electron binding energy $E_e = E_p - \phi$ where E_e is the energy of the ejected photon, E_p is the photon energy and ϕ is the binding energy of the electron. Photoelectric interactions are more common with lower energy photons and are highly dependent on the photon energy. The probability of photoelectric interaction varies with E^{-3} [56].

FIGURE 4 Photoelectric effect

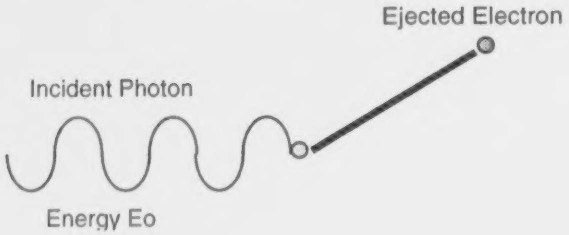

1.5 Effects of Attenuation and Scatter

For a 20% energy window centered around 140 keV, as many as 30% of the photons detected will have undergone one or more scatter interactions. Scatter is also highly dependent on the source distribution and location and the shape and structure of the scattering object. The detection of scatter event can cause a considerable degradation in the quality and resolution of the recorded image. The effect of scatter is to contribute additional counts to the image. However, the detection and emission locations for the scattered photons are usually not correlated so that scattered photons do not provide any information on the distribution of the radioisotope being imaged. The dependence on the imaging geometry and object composition makes removing scattered events a major problem in SPECT imaging.

For the 140 keV photons emitted by Tc-99m, approximately 50% of the photons will be absorbed by 5 cm of water. The magnitude of the attenuation and scatter problem in SPECT is easily illustrated by acquiring a SPECT study of a uniform water phantom filled with a uniform concentration of activity. In the reconstructed SPECT images, there is a marked decrease in the reconstructed activity in the central regions relative to the outer rim of the phantom. This is sometimes called the "hot-rim effect" and is illustrated in Figure 5 below.

FIGURE 5 Reconstructed SPECT slice of a uniform water phantom

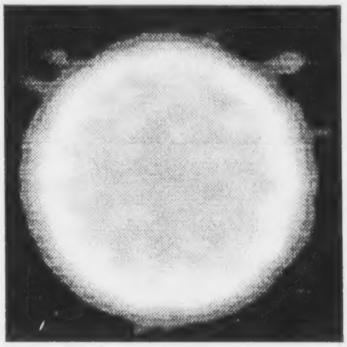

As can be seen in this image, there is an obvious ring of activity around the periphery of the water phantom, with a decrease in activity towards the center. The magnitude of this attenuation/scatter effect is more dramatically illustrated by a line profile through the center of the image (Figure 6) where the number of reconstructed counts in the central region is almost half of those towards the edge of the phantom. With just photon attenuation alone, the counts in the center of the phantom would be considerably less, about 15-20% of the counts around the edge. That the central region is only 50% lower than the edge is an indication of the contribution of scatter to the SPECT image.

FIGURE 6 Profile through the center of the image in Figure 5. The center of the phantom is pixel 64.

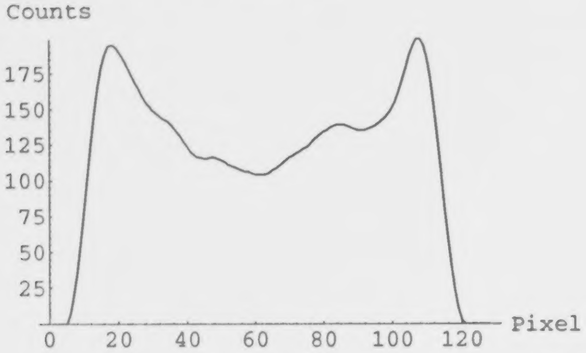

The effects of attenuation are particularly evident in brain, cardiac and liver imaging, which involve imaging regions located deep within the body and surrounded by several types of tissue with different attenuation coefficients. In head imaging, attenuation is caused by brain tissue as well as the surrounding skull. It has been shown that the skull will reduce the reconstructed count density at the edges because of the oblique path of photons through the bone [5]. Variations in skull thickness can cause differences in the reconstructed activity between different areas of the brain. Reconstructed count differences of around 6% between parietal-occipital and frontal-temporal regions due to variations in skull thickness has been shown [6]. Even the head holder used can cause a significant variation in counts.

The liver is a large organ in the abdomen which lies relatively close to the surface, yet also extends deep into the abdomen. In liver SPECT, the periphery of the liver is well defined, but a gradual decrease in counts towards the interior can be readily observed, making the detection of central lesions more difficult [7].

One of the areas to which attenuation correction has been investigated and applied extensively is cardiac imaging[23, 31, 37, 38, 40]. Performing attenuation correction on cardiac SPECT images presents a number of problems. The chest region contains muscle, bone, lung, and soft tissue, all of which have different attenuation coefficients. Applying attenuation correction methods which assume a uniform attenuation coefficient distribution will create unacceptable artifacts. The heart is also situated slightly left of the mediastinum, so some views are attenuated by more tissue than others. The spinal column and sternum also attenuate photons significantly. For this reason, typical cardiac SPECT acquisition protocols cover a 180° or 240° arc generally from the right anterior oblique to left posterior oblique views. This avoids views through the spinal column and through the right lung which could introduce artifacts in the reconstruction due to increased attenuation [59, 60]. Breast tissue can cause low count density artifacts and streak artifacts in images of the anterior wall of the heart because of the extra thickness of tissue. The size and magnitude of the anterior wall artifacts can vary with breast size and position [9]. Attenuation due to the diaphragm can result in decreased counts in the inferior wall of the heart.

CHAPTER 2

Attenuation Correction Algorithms

2.1 Exponential Radon Transform

The Radon transform is a mathematical construct which maps any function f(x,y) onto a set of line integrals **R**, and can be used to model the SPECT data collection process for the case of no attenuation and scatter. In the case of SPECT imaging, the Radon transform represents the summation of the activity along a line from the detector through the object at angle θ.

$$g(x,\theta) = \int_R f(x,y) \qquad \text{(EQ 6)}$$

Here, **R** is the set of lines which the line integrals are evaluated on. The radioisotope distribution is described by the function f(x, y) and the SPECT projections by g(x,θ). The (x,y) coordinate system used is set up so the axes are parallel (x) and perpendicular (y) to the detector face at angle θ.

The exponential Radon transform (Figure 7) is a generalization of the Radon transform in which the sum is modified by an exponential term. The attenuated Radon transform models the projection process in SPECT as a set of line integrals over the radioisotope distribution weighted by an exponential factor describing the attenuation due to the body [10] (ignoring scatter)

$$g(x,\theta) = \int_R f(x,y)\, e^{-\mu t} dy \qquad \text{(EQ 7)}$$

The effect of attenuation is described by the exponential factor $e^{-\mu t}$ where t is the distance from point (x,y) to the edge of the body contour and μ is the linear attenuation coefficient of the object. Equation 7 describes a simple case where the attenuating object is a uniform object with linear attenuation coefficient μ. In reality, most objects (patients) are quite heterogeneous in their composition and the linear attenuation coefficients vary significantly from region to region. The attenuated Radon transform is easily modified to include non-uniform attenuation as shown in the equation below [11]

$$g(x,\theta) = \int_R f(x,y)\, exp\left(-\int_L \mu(x,y')\, dy'\right) dy \qquad \text{(EQ 8)}$$

where $\mu(x,y)$ represents the distribution of attenuation coefficients within the body. The integral in the exponential term, $s(x,\theta) = exp\left(-\int_L \mu(x,y')\, dy'\right)$ is evaluated over the set of lines **L** from the point (x,y) to the edge of the body contour (the surface) as illustrated in Figure 7.

FIGURE 7 Geometry for the attenuated Radon transform.

$$s(x,\theta) = exp\left(-\int_L \mu(x,y)\,dy\right)$$

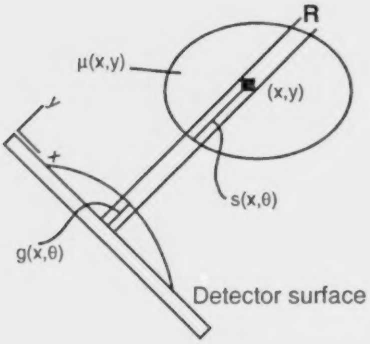

The goal of image reconstruction in SPECT is to obtain the radioisotope distribution, f(x,y) given the set of projections g(x,θ). To provide an accurate reconstruction of the radioisotope distribution, photon absorption and scatter must be taken into account during the reconstruction process. One of the problems which makes this difficult is that attenuation and scatter depend on the size and composition of the body, the location of the source within the body, and the distance of the source to the detector. Because of the complexity of the attenuation and scatter problem, they are generally handled separately although in reality, attenuation and scatter are tightly integrated. For the purposes of this project the scatter problem will be neglected for simplicity, although any attempt at performing accurate SPECT reconstruction must take scatter into account.

Several methods have been developed for performing attenuation correction on SPECT images. All correction methods can be grouped into 3 general categories; pre-processing, intrinsic, and post-processing, depending on whether the attenuation correction occurs before, during or after the reconstruction. Many correction methods currently used assume a uniform attenuation coefficient throughout the body for computational simplicity, but a number of methods have been developed which can correct for non-uniform attenuation through the use of a non-uniform attenuation map.

The development of each algorithm requires assumptions be made about the source distribution in the attenuating object, as well as the shape and size of the attenuating object.

2.2 Pre-reconstruction Correction

In pre-processing methods, the raw projections are corrected with a correction factor prior to the reconstruction. A correction factor derived by considering a point source or uniformly distributed source in a uniform attenuator is used to correct the geometric mean

$$P = \sqrt{P_1 \times P_2} \qquad \text{(EQ 9)}$$

or arithmetic mean

$$P = \frac{P_1 + P_2}{2} \qquad \text{(EQ 10)}$$

of two opposing projections, P_1 and P_2. The correction factor is usually a multiplicative factor determined from an assumed attenuation coefficient and body contour and assumptions about the source distribution. The corrected projections are then reconstructed using standard filtered backprojection algorithms. The method is fast and simple to apply, however there are problems with the geometric and arithmetic mean methods because of their dependence on source depth, source thickness and body contour. Errors are also introduced if the source distribution is non-uniform. The geometric mean is also particularly susceptible to noise, and will produce streak artifacts if the data is noisy [1]. Despite these problems, the geometric and arithmetic mean methods are still widely used because of their simplicity and ease of use.

2.3 Postprocessing Correction

Post-processing algorithms apply attenuation correction to the reconstructed images. The most popular method is an algorithm developed by Chang [12]. Chang's algorithm was derived by considering the projection and reconstruction of a point source in a uniform attenuator. The reconstructed images are multiplied by a correction matrix calculated from the equation

$$C(x, y) = \frac{1}{\frac{1}{M}\sum_{i=1} exp(-\mu l_{\theta_i})} \qquad \text{(EQ 11)}$$

where M is the number of projections, and l_θ is the distance from point (x,y) to the body contour at angle θ. This correction factor is an average of the attenuation factors over all the projection angles. Chang's correction method is exact for a point source but if the source is a distributed source and attenuation is non-uniform, the correction matrix produces regions that have been over-corrected and other regions which have been under-corrected depending on how the source is distributed in the object [12]. To get around this problem, the

Chang algorithm can be iterated one or more times using the following procedure. The corrected projections are reprojected to obtain a new set of projections, P_{new}. These are subtracted from the original projections to obtain a set of error projections, which are then reconstructed to produce a set of error images. The correction matrix is applied to the error image, and then added to the corrected projections P_{new} to form the corrected images. Because of the heavy computational requirements, the Chang algorithm is usually not iterated or iterated only once. In most applications, the Chang method is not iterated at all since a single application is usually considered to be sufficient. The Chang method can also be adapted for non-uniform attenuation by modifying the exponential term to reflect a spatially varying attenuation map [19, 50].

2.4 Intrinsic Correction

Intrinsic attenuation correction algorithms incorporate the attenuation correction into the reconstruction process. Intrinsic correction algorithms are generally attempts at finding a solution to the Radon transform. Tretiak and Metz [10] derive an inversion formula for the Radon transform in which the projection data is multiplied with an exponential factor related to the object size.

$$p_m(x|\theta) = p(x|\theta)\,exp(\mu L) \qquad \text{(EQ 12)}$$

Here, L is the y distance to the edge of the body contour (with the origin placed at the center of rotation of the camera heads), $p(x \mid \theta)$ are the original projections and $p_m(x \mid \theta)$ are the modified projections at angle θ. The results are then backprojected using an exponential weighting factor to correct for attenuation. However, the method tends to amplify noise in the reconstructed images.

In an approach used by Tanaka [13, 41], the modified projections are filtered with a modified convolution function designed to reduce image distortion and noise. The filtered projections are then backprojected with exponential weighting factors determined for a point source in a uniform attenuator. Tanaka's method requires that several reconstruction and filtering parameters used to determine the weighting factors be determined in advance. These parameters are chosen to optimize the noise characteristics and minimize distortion of the reconstruction for certain geometries. Computer simulations of Tanaka's method showed fairly accurate reconstructions for small objects but exhibited increasing sensitivity to the correction parameters when applied to objects with large attenuating geometries.

In order to deal with non-uniform attenuation, Tanaka's weighted backprojection method was modified so that the projections were multiplied by an exponential factor determined from a non-uniform attenuation map [14]. The exponential factor $e^{\mu L}$ in Equation 12 is replaced with a summation $exp\,(\sum_{L} \mu_i d_i)$ where μ_i is the discrete representation of the attenuation map and d_i is the path length in pixel i.The weighting factors used in the backprojection step are also calculated using the attenuation map. The use of a non-uniform attenuation map improved the reconstructions, but still amplified noise and introduced some non-uniformity artifacts [14].

2.4.1 Iterative Algorithms

More recent iterative algorithms have been developed to improve the quantitative accuracy of SPECT reconstructions. Iterative algorithms start with an estimate of the source distribution (the first guess is usually a uniform distribution), reproject it, and then compare the estimated projections with the acquired projections. From the comparison, a set of error projections is obtained which is then backprojected, usually with weighting factors which incorporate one or more of attenuation, scatter, detector and geometric response. The reconstructed error images are then used to correct the current estimate to create a new estimate of the source distribution. Projector/backprojector pairs which incorporate scatter/attenuation effects and geometric response functions in order to more accurately model the SPECT acquisition process have been written to improve the accuracy of iterative reconstruction techniques [11].

In maximum likelihood expectation maximization (MLEM) methods [3, 15, 42, 47], the SPECT data collection process is modelled as a statistical process. Projection data are modelled taking into account the statistical nature of the emission process, and considering the effects of scatter, attenuation and detector response. A projector/backprojector pair also incorporating these effects is used as well. An initial assumption about the radioisotope distribution is used, and subsequently modified by iterating the method to produce a radioisotope distribution that is most likely to produce the observed projection data. This process is described by the following equation obtained from [15],

$$\hat{\lambda}^{(i)}(x) = \hat{\lambda}^{(i-1)}(x)\,[1 + \eta^{(i-1)}(x)] \qquad \text{(EQ 13)}$$

where $\hat{\lambda}^{(i)}(x)$ and $\hat{\lambda}^{(i-1)}(x)$ are the current and previous estimates of the source distribution and $\eta^{(i-1)}(x)$ is a correction term. The exact form of the correction term is given in [15], and involves terms describing the survival probability of emitted photons and the error between the measured data and the projection of the ith iteration.

The MLEM algorithm can also be extended into three dimensions as well to do three dimensional reconstructions. One of the advantages that makes MLEM methods appealing is the ability to incorporate effects such as attenuation, scatter and detector response. The algorithm is very computationally intensive, often requiring many iterations before a suitable estimate of the radioisotope distribution is achieved. With the increasing power of computers being used in SPECT, this is now becoming less of a problem. There is a tendency for the noise level in the images to increase with large numbers of iterations, but the method has been shown to provide accurate and quantitative reconstructions [15, 43].

2.5 Non-uniform Attenuation Correction

One of the problems with current attenuation methods is that most of them approximate the body with a uniformly attenuating ellipse. The obvious problem with this approximation is that the body is made up of several different tissue types, with varying attenuation coefficients. In areas such as the chest, the body is very non-uniform, and applying a uniform attenuation to

SPECT images acquired from the chest can cause artifacts. To remedy the problem, a non-uniform attenuation map which accurately describes the distribution of attenuation coefficients is required. A non-uniform attenuation map can be obtained from a transmission scan of the patient, either separately or simultaneously with the SPECT study. Several attempts have been made to use X-ray CT scans for the attenuation map, but this creates problems of image registration and requires the conversion of CT (Hounsfield) numbers to linear attenuation coefficients [16] as well as additional radiation exposure to the patient. A common approach is to use an external point, line or flood source attached to the SPECT gantry opposite a gamma camera to obtain an attenuation map. The external source is used to measure the photon transmission through the body, and with some processing can be used to obtain an accurate attenuation distribution. Most correction methods assuming uniform attenuation are easily adapted to use a non-uniform attenuation map.

2.5.1 Transmission SPECT Isotopes

One thing that must be considered for transmission and emission SPECT is the choice of radioisotope to use for the transmission study. If the transmission study is to be acquired separately from the SPECT study, the radioisotope used can be the same as that used for the SPECT study. Since linear attenuation coefficients are energy dependent, one of the benefits of using the same radioisotope for transmission and emission scans is that the calculated attenuation coefficients do not need to be converted to the attenuation coefficients of the emission isotope. However, the need to acquire a separate study increases the patient scan time and the possibility of patient motion between the separate scans.

If the transmission study is acquired simultaneously with the SPECT study, a different radioisotope is generally required for the transmission source if a single headed camera is used, but not if a multi-headed camera is used (this situation is discussed later). The transmission data is acquired using one energy window, while the SPECT data is acquired in a second energy window. In general, the transmission source is chosen to have a lower energy than the emission source to avoid contaminating the SPECT study with unrelated photons. A simultaneous acquisition has the benefit of not adding any extra time to the scan, avoiding image registration problems and eliminating problems with motion between two separate scans. Unfortunately the attenuation coefficients achieved from the transmission study need to be converted to the energy of the emission source. Also, a correction needs to be done for crosstalk between the emission and transmission energy windows. Photons from the higher energy isotope can be scattered and detected in the lower energy window, contaminating the data collected in the lower energy window. This contamination must be removed prior to reconstructing the images.

Some of the transmission sources that have been investigated for use are Gd-153, Am-241 and Tc-99m. Both Am-241 and Tc-99m have been investigated for Tl-201 cardiac SPECT [17] while Gd-153 has been tried for Tc-99m imaging. Gd-153 is an appealing source because of its long half life (242 days) and gamma emission energies (98 and 103 keV). For Tl-201 cardiac SPECT, Am-241 is appealing because of its 59.4 keV gamma emissions and very long half life (432.2 yr). Since the energy windows for Tl-201 and Am-241 overlap, crosstalk between the energy windows must be corrected for. Am-241 provides high bone-tissue contrast although the attenuation coefficient for bone determined from the Am-241 attenuation map was not quite accurate because of the requirement for linear interpolation from the transmission energy to the emission energy [17]. Despite this, Am-241 has been shown to be a viable transmission source for Tl-201 cardiac SPECT. The usefulness of Tc-99m/Tl-201 and Gd-153/Tc-99m combinations of transmission/emission sources has been investigated in a recent paper by Welch et. al [18]. They found that Tc-99m produced more accurate attenuation maps than Gd-153 but for both combinations, scaling the attenuation coefficients from the transmission energy (Tc-99m or Gd-153) to values appropriate for the emission energy (Tl-201 or Tc-99m) resulted in inaccuracies in the attenuation map. However, more phantom studies are required to determine the optimum transmission/emission source combination.

These problems can be avoided in multi-headed SPECT systems. For these systems, one head is set to view the transmission source, and the other head(s) set to view the emission source. This allows the same radioisotope to be used as both emission and transmission source. Both emission and transmission studies can be acquired simultaneously. There is no scaling required for the attenuation coefficients determined. Tc-99m is also inexpensive and easy to obtain in a clinical setting.

Once the transmission study is acquired, it must be converted to a ray sum of attenuation coefficients using the equation

$$\sum \mu_i = ln\left(\frac{I_o(x,y)}{I(x,y)}\right)\frac{1}{\Delta x} \qquad \text{(EQ 14)}$$

where $I_0(x,y)$ is the intensity of the transmission source with no objects in the beam, $I(x,y)$ is the amount of radiation transmitted through the object as measured by the gamma camera and Δx is a scaling factor related to the voxel dimensions. This equation assumes a narrow beam geometry (no scattered photons detected in the transmitted beam). The resulting $\sum \mu_i$ can then be reconstructed using a variety of algorithms.

2.5.2 Transmission Source Geometries

One method of acquiring an attenuation map is to use an external flood source mounted opposite a single gamma camera using parallel hole collimators [19, 35]. This method is suitable for single head SPECT systems and requires some hardware modification to the camera to support the source. If a simultaneous transmission/emission study is to be performed, this technique requires two different isotopes for the transmission and emission sources. If only a single source is used, the transmission and emission studies must be performed sequentially.

FIGURE 8 Flood source - parallel hole collimator geometry

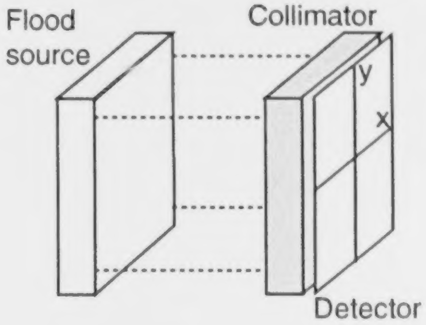

By using a different radioisotope than the one used for the emission study (Gd-153 or Co-57 for example), the transmission study can be acquired simultaneously with the SPECT study with no increase in scan time. The transmission source is generally chosen to have a lower photon energy than the emission source to avoid contaminating the SPECT study with scattered transmission photons. As a result, some form of scatter correction must be performed on the transmission study to correct for the detection of scattered emission photons in the transmission window i.e. scattered events from the higher energy window (emission) being detected in the lower energy window (transmission). Bailey et al [19] employ a convolution technique applied to the geometric mean of the opposing emission images to predict the scatter contribution from the emission source to the transmission images. Almquist et al [35] use build up factors determined from Monte Carlo simulations to correct the transmission maps for scatter. Both techniques perform well at removing scattered photons, but neither addresses the problem of incorrectly located scatter photons. It is also useful to collimate the flood source in some way to reduce scatter and improve the resolution of the images [61]. There are several drawbacks to using a flood source. Flood sources tend to be large and somewhat cumbersome, and require a relatively large amount of activity (~1.5 GBq). They must also be shielded when not in use. Unless the source is collimated, there is a considerable amount of scatter included in the transmission images. Using a flood source also requires that a different radioisotope be used.

Other investigators have used a line source in conjunction with parallel hole collimators [20, 21].

FIGURE 9 Scanning line source - parallel hole collimator geometry

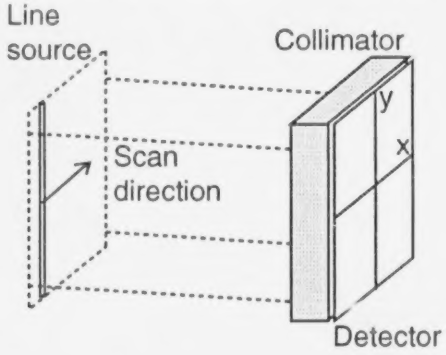

The line source is mounted opposite the camera head and scanned across the FOV with a computer controlled stepping motor. The line source is highly collimated to a narrow beam so that only a small portion of the camera is illuminated. To acquire the transmission scan, the camera is collimated electronically so that data for the transmission scan is acquired only for the region of the head being illuminated by the source as it moves across the camera. The emission window is turned off where the transmission window is active. One of the advantages of a scanning line source is that any combination of transmission/emission sources can be used. The electronic collimation of the camera and tight collimation of the line source serve to limit the number of scattered photons detected in each energy window. Attenuation coefficients reconstructed using the tightly collimated line source more closely approximate narrow beam attenuation coefficients, indicating that the transmission data is relatively scatter free. However, in order to provide a sufficient photon flux, a large amount of activity is required for the line source (6 GBq). It has also been suggested that a non-uniform line source distribution may reduce the amount of noise in the attenuation maps. Computer simulations showed that attenuation maps determined from a line source distribution which was the inverse of the average photon transmission through the chest showed a large reduction in noise level [21].

Another method uses cone beam collimators (circular or rectangular), which focuses to a point above the collimator surface. A point source can be mounted at the focal point of the collimators as illustrated below [22, 36].

FIGURE 10 Point source - cone beam geometry

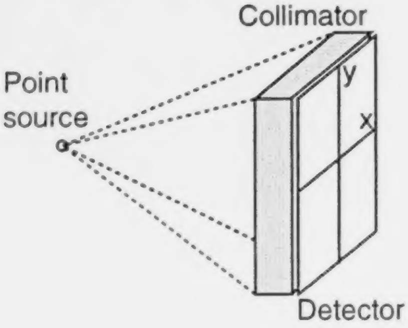

An advantage of using cone beam collimation is the high sensitivity, which allows a low transmission source activity to be used (74 MBq) and short scanning times. The cone beam collimation also provides very high resolution attenuation maps. Cone beam geometry can also be obtained without the use of a collimator, since the detection geometry for a point source is still a cone beam. This offers an additional increase in sensitivity, but at the price of increased scatter. One of the problems with cone beam collimation is that the data set collected using conventional circular scanning orbits is insufficient to provide a complete reconstructed image due to truncation of the object in the axial direction. In order to acquire a complete set of data, a more complex orbit is required such that any plane through the region being reconstructed is intersected by the trajectory of the focal spot [23]. Cone beam collimators also require special reconstruction techniques in order to properly reconstruct the SPECT distribution.

Another more clinically practical method is to mount a collimated line source opposite a gamma camera with a fan beam collimator attached [24, 30, 39]. This is the approach used in this project.

FIGURE 11 Line source - fan beam collimator geometry

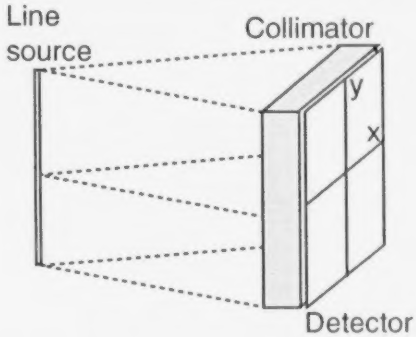

The line source is mounted at the focal line of the collimator and moves opposite the camera around the patient. The amount of activity required in the line source is relatively low, about 370 MBq. This approach is easily applied especially to triple headed SPECT systems. One of the big advantages of triple head systems is a short scan time, since each head only needs to rotate through a 120° arc. To do transmission CT with a triple head system, a highly collimated line source can be mounted between two of the heads so that only the one opposing head is illuminated. The other two heads "see" only the emission source, while the third head "sees" both the emission and transmission sources. The radioisotope selected for the transmission scan can be the same or different from the emission radioisotope. If the radioisotopes are the same, isolating the transmission scan is a simple matter of subtracting the emission data gathered by the other two heads from the combined emission/transmission data gathered by the third head. The transmission study is then converted to attenuation coefficient ray sums and reconstructed to provide an attenuation map.

One of the disadvantages of this technique is that since only one transmission source is used, each head must rotate through 360° in order to acquire a complete transmission data set, making the total acquisition time longer. Placing a transmission source opposite each head would eliminate this problem, but this would then require the transmission source to be different from the emission source. Truncation of the transmission source can also be a problem, especially when the body is being imaged. The smaller head size usually found on triple headed cameras combined with the fan beam collimators can result in severe truncation artifacts when applied to the body. Selecting fan beam collimators with a longer focal length can help reduce the truncation problem, but if the focal length is too long, the transmission source will be truncated by the two adjacent heads.

2.6 Scatter Correction

In order to perform truly quantitative SPECT, the scatter problem must also be considered. Although scatter correction will not be performed within the scope of this project in order to keep things simple, scatter correction is sufficiently important to merit a brief discussion of some correction methods [62].

The most commonly used method is to employ a narrow energy window around the photopeak. The typical energy window used is 15-20% and is usually centered around the photopeak, but in some cases shifted towards a slightly higher energy (asymmetric). This method rejects most of the higher order scattered photons with energies outside the photopeak window, but some low order scattered photons (photons which have scattered only once or twice) with sufficient energy to be detected in the photopeak window are still detected.

One method is to acquire a SPECT image in an energy window just below the main photopeak window. This scatter image is then used to estimate the amount of scatter in the main photopeak window by convolving with a scatter function or scaling with some mean scatter fraction and then subtracting the result from the photopeak image.

Other methods include filtering and using effective attenuation coefficients to account for scatter. Both the Metz and Wiener filter implicitly perform some scatter correction through their use of the system MTF and object power spectrum. The effective attenuation coefficient performs both scatter and attenuation correction by using an attenuation coefficient that is slightly lower than the narrow beam attenuation coefficient to perform attenuation correction. The idea behind this is that since the detection of scattered events contributes to the total transmission through the object, the apparent attenuation coefficient is lower than the actual narrow beam attenuation coefficient. Therefore, a lower attenuation coefficient should be used to perform the attenuation correction. For the case of 140 keV photons, an effective μ for water of 0.12 cm^{-1} is generally used, rather than the actual value of $\mu=0.15$ cm^{-1}.

In more recent methods, reconstruction algorithms have been developed (i.e. maximum likelihood methods) which are capable of accurately modelling the SPECT acquisition process by incorporating scatter, attenuation and detector response into the forward and backprojection portions and the comparison stage. Taking these effects into consideration will make SPECT reconstructions more accurate and quantitative.

CHAPTER 3

Reprojection Correction Algorithm

3.1 Rationale

The purpose of performing attenuation correction is to improve the quality and accuracy of SPECT reconstructions. Without attenuation correction, reconstructed images suffer from reduced count density in the central regions. This can reduce the contrast and visibility of centrally located lesions in the SPECT images. Attenuation can also cause low density artifacts especially if the attenuating medium is highly non-uniform such as in the chest. To provide truly accurate SPECT reconstructions, the problem of scatter must also be considered. However, for simplicity, scatter will be neglected and only the attenuation problem will be considered.

In this section, a simple and relatively quick method of performing non-uniform attenuation correction is presented and investigated. To begin, a conceptual description of the method to be developed is given. This will be followed by a more thorough development of the correction algorithm.

The method is based on performing attenuation correction on the projection of each pixel in the reconstructed image using a non-uniform attenuation map to determine the appropriate attenuation correction factors. Consider a uniform activity distribution with an activity concentration of A within a uniformly attenuating object with attenuation coefficient μ. Let P represent the set of SPECT projections of A, and let C be the SPECT images reconstructed from P. Because of attenuation, each voxel element within A contributes $A exp(-\mu l)$, where l is the distance from the voxel to the edge of the attenuating object for a given projection angle, to the projections P. If the precise distribution of A were known in advance, then performing attenuation correction would be a simple matter of multiplying each of these contributions to P by the inverse of the exponential, $exp(\mu l)$. However, in practice, $A exp(-\mu l)$ is not known. Consider the reconstructed SPECT images, C. If C is forward projected by performing a simple Radon transform, then this should reproduce the projections P (since C was obtained by backprojecting P). Since P is simply the accumulation of $A exp(-\mu l)$ for all voxels, this suggests that the projection of each voxel element of C can be used to estimate $A exp(-\mu l)$. Therefore, multiplying the projection of each voxel element of C by $exp(\mu l)$ should produce a new set of attenuation corrected projections which can then be reconstructed to reproduce A. A more detailed explanation of this algorithm is provided below.

3.2 Derivation

For simplicity, only the two-dimensional case is considered. The x-y coordinate system is oriented parallel and perpendicular to the detector plane as illustrated in Figure 12. Parallel hole collimation is assumed for simplicity, although any type of collimation could be used with appropriate modifications to the projection geometry.

Let A(x,y) represent an arbitrary two dimensional radioisotope distribution within an attenuating material described by the function $\mu(x,y)$. The set of SPECT projections of this radioisotope distribution neglecting scatter and detector response effects can be ideally described by the attenuated Radon transform

$$P(x|\theta) = \int_0^{\infty} A(x,y)\, exp\left(-\int_y^{y_d} \mu(x,y')\, dy'\right) dy \qquad \text{(EQ 15)}$$

where $P(x|\theta)$ is the projection profile at angle θ and y_d is the position of the detector plane. The integral in the exponential is carried out along a line perpendicular to the surface of the detector from the current pixel y to the detector plane at y_d. The attenuated Radon transform is illustrated in Figure 12 below.

FIGURE 12 Attenuated Radon transform projection geometry

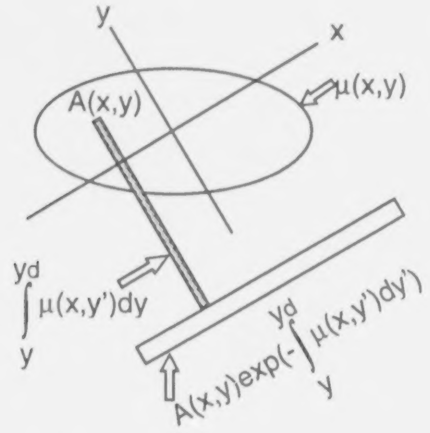

For the purpose of this derivation, consider the projection process on a pixel by pixel basis, again assuming the two dimensional case and the same geometry illustrated in Figure 12 and parallel hole collimation. The contribution each pixel in the source distribution makes to the projection data in projection bin i is given by

$$p_i = A_{ij} exp \left(- \sum_{j'} \mu_{ij'} d_{ij'} \right) \qquad \text{(EQ 16)}$$

where p_i is the attenuated projection of A_{ij} into projection bin i, A_{ij} and μ_{ij} are the discrete representations of the source (A(x,y)) and attenuation distributions (μ(x,y)) respectively, and $d_{ij'}$ is the distance through each pixel intersected by the ray (Figure 13) between pixel (i, j) and projection i.

FIGURE 13 Pixel intersection length for one pixel

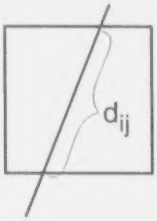

The complete projection profile is given

$$P_i = \sum_j A_{ij} exp(\sum_{j'} -\mu_{ij'} d_{ij'}) \qquad \text{(EQ 17)}$$

In the absence of attenuation, the contribution p_i^* of each pixel to the projection would simply be given by

$$p_i^* = A_{ij} \qquad \text{(EQ 18)}$$

The unattenuated contribution of each source pixel to the projections, p_i^*, can be obtained by multiplying both sides of Equation 16 by the inverse of the exponential factor,

$$A_{ij} = p_i exp(\sum_j \mu_{ij} d_{ij'}) \qquad \text{(EQ 19)}$$

so that a set of attenuation corrected projections P^*_i would be given by

$$P^*_i = \sum_j A_{ij} = \sum_j p_i exp(\sum_j \mu_{ij} d_{ij'}) \qquad \text{(EQ 20)}$$

which is just the discrete Radon transform of A_{ij}. What is required at this point is a way to estimate the contribution of each pixel element p_i in Equation 16 to the projection data.

Let C(x,y) represent the filtered backprojected image reconstructed from the set of projections given by P(x,θ) described by Equation 17. If we forward project these images (i.e. apply the Radon transform), we would get a set of projections, $P'(x, \theta)$

$$P'_i = \sum_j C_{ij} \quad \text{(EQ 21)}$$

where C_{ij} is the discrete representation of the reconstructed radioisotope distribution. The contribution from each pixel in C_{ij} is then

$$p'_i = C_{ij} \quad \text{(EQ 22)}$$

Assuming that the projection and backprojection operations are inverses of each other, we can say $P'(x, \theta) = P(x, \theta)$ or

$$\sum_j A_{ij} exp\left(-\sum_{j'} \mu_{ij'} d_{ij'}\right) = \sum_j C_{ij} \quad \text{(EQ 23)}$$

This assumption is technically not true, since a simple backprojection of the Radon transform of a function f(x,y) results in the original function blurred by a point spread function (PSF) [25] proportional to 1/r, where r is the distance from the image pixel (x,y) being backprojected. However, it may be a reasonable approximation to make since the ramp filter used in filtered backprojection (FBP) routines used to reconstruct images is intended to compensate for the 1/r blurring introduced by the backprojection process.

If p'_i, which is the contribution of each pixel in C_{ij} to the set of projections P'_i (Equation 22), is used as a guess for p_i in Equation 16 this gives the following equation (substitute Equation 22 into Equation 19)

$$A_{ij} = C_{ij} exp\,(\sum_{j'} \mu_{ij'} d_{ij'}) \qquad \text{(EQ 24)}$$

This suggests the following method to correct for attenuation correction:

1. Acquire and reconstruct a transmission and emission study to obtain C_{ij} and μ_{ij}.
2. Project each pixel in C_{ij} and multiply by $exp\,(\sum_{j} \mu_{ij} d_{ij})$ to get a set of corrected projections.
3. Reconstruct the corrected projections.

The implementation and use of the method developed here is described and investigated in the following chapters.

CHAPTER 4

Materials and Methods

4.1 Picker PRISM 3000 SPECT system

The usefulness of the method developed in the previous chapter was investigated on a Picker PRISM 3000[1] triple head SPECT system.

FIGURE 14 Picker PRISM 3000 SPECT gantry

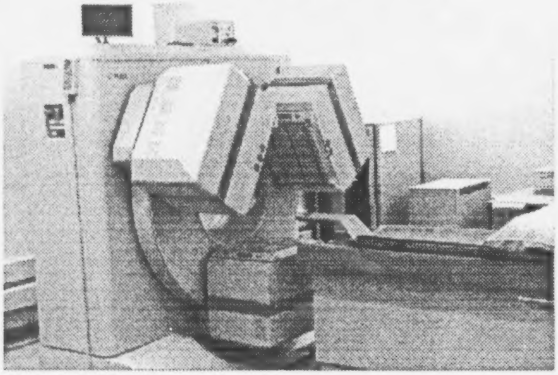

---

[1] Ohio Imaging, Picker International, Bedford Heights, Ohio

The system consists of a triple head SPECT gantry, with a separate acquisition module, dedicated reconstruction accelerator and an Odyssey computer system with two CPUs. Each detector has a field of view of 40 cm x 24 cm. The heads are arranged in a triangular configuration. Low energy ultrahigh resolution fan beam collimators (LEUHR-FAN) with a focal length of 50 cm are mounted on each head. Projection data is acquired by a separate acquisition processor and stored on the Odyssey computer. Reconstructions are carried out on the dedicated reconstruction accelerator using standard filtered backprojection algorithms.

4.2 Line Source/Holder Assembly

To acquire the transmission images, a fillable line source[1] located at the focal line of the collimator was used for the transmission source. The line source (Figure 15a) has a total length of 45.7 cm, with a useful length of 38.1 cm. The inner tubing is 1.2 mm in diameter and is surrounded by a plastic shell for support.

The line source was mounted to the gantry turret using a specially designed bracket and holder (Figure 15b) constructed out of aluminum. The bracket was designed so that the source holder could be moved up and down to position the source at the focal line of the collimators. The source holder is fixed in place by tightening two knobs on the bracket. Graduated markings allow the source holder to be positioned at the nominal focal distance of the collimators used. Radial motion during the scan is not possible with the source holder, so only circular orbits are possible. The aperture of the source holder was lined with lead and collimates the line source to a fan angle of 40° so that only head 1 is illuminated (Figure 16). There is no source collimation along the axial direction. The source holder can also be removed when not in use so that it is not in the way for other patient studies.

---

[1] Data Spectrum Line Fixture Model 1800, Data Spectrum Corp., Chapel Hill, NC

FIGURE 15

a) Data Spectrum line source

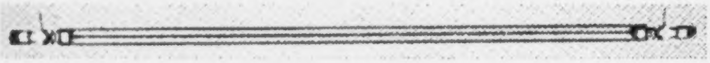

b) Line source/holder assembly mounted on the SPECT gantry

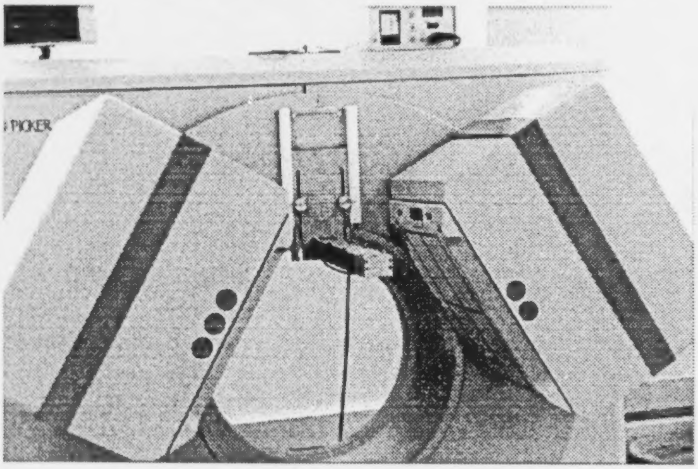

FIGURE 16 Schematic of the line source setup.

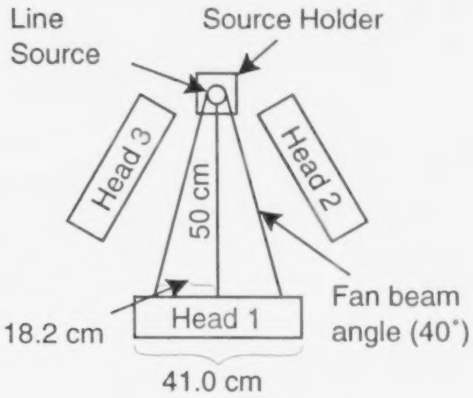

4.3 Phantoms

4.3.1 Linearity Phantom

To produce accurate attenuation maps, the reconstructed pixel values have to be correlated to linear attenuation coefficients. To verify this, a linearity phantom was developed and tested. The base phantom was a CT linearity phantom consisting of 3 plastic inserts of different densities: a low density translucent insert, a clear medium density insert and a white high density insert. In addition, two cylindrical acrylic and simulated bone inserts, rectangular Perspex and aluminum inserts and an IV bag were added to the phantom to increase the range of attenuation coefficients used to establish the linearity relationship. Figure 17 below shows the layout of the test objects used.

FIGURE 17 Cross section of inserts in the linearity phantom: 1) simulated bone 2) low density plastic 3) Perspex 4) medium density plastic 5) acrylic 6) water 7) high density plastic 8) aluminum

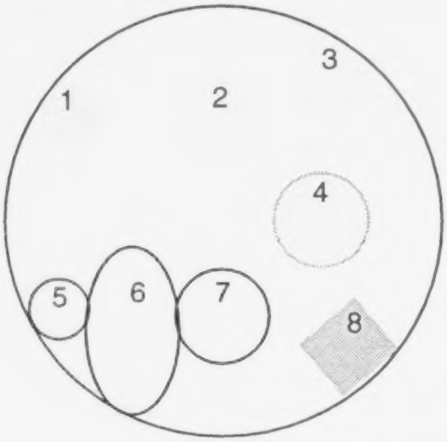

4.3.2 Uniformity Phantom

The uniformity of the transmission maps was tested using a uniform water phantom with and without activity. The phantom, shown in Figure 18, is a fillable circular cylinder 19.5 cm in height and 21 cm in diameter.

FIGURE 18 Uniform water cylinder

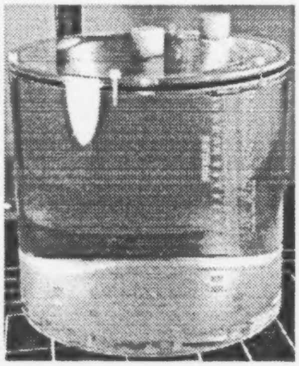

4.3.3 Resolution Phantom

To investigate the spatial and contrast quality of the transmission images produced by this system, images of a Jaszczak phantom[1] were taken. The Jaszczak phantom is a fillable circular cylindrical phantom, 21.6 cm in diameter and 18.6 cm in height, with sections that can provide information on the contrast and resolution of a SPECT system (Figure 19). One section consists of 6 solid spheres of different radii. The other section consists of 6 pie shaped sections made up of rods of different sizes: 4.8, 6.4, 7.9, 9.5, 11.1 and 12.7 mm. Only the section with the rods was scanned to get an idea of the attainable resolution of the attenuation maps. To provide maximum contrast, the Jaszczak phantom was scanned empty (i.e. with no water).

FIGURE 19 Jaszczak phantom

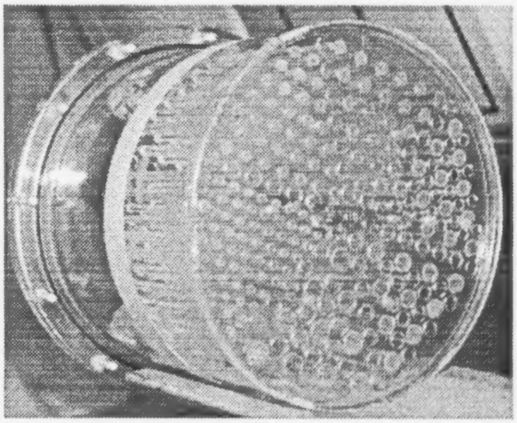

---

[1] Data Spectrum Phantom Model 5000, Data Spectrum Corp., Chapel Hill, NC

4.3.4 Brain Phantom

A brain phantom was created to examine the qualitative properties of the reprojection correction method. The brain phantom consisted of a human skull filled with inserts. The brain cavity of the phantom was filled with a soft tissue equivalent mixture of beeswax and paraffin. The "brain" consisted of two parts, one filling the bottom portion of the skull cavity in which the inserts were embedded, and a removable "cap" filling the remainder of the skull cavity. The phantom had five inserts each containing a small amount of activity (1.5 MBq/cc) which were used to simulate activity in the frontal and temporal lobes and the cerebellum. The inserts were made from 35 mm film cannisters with solid nylon plastic inserts. The amount of activity in each insert is shown in Table 1 below.

TABLE 1 Brain phantom insert activity

Insert	Activity (MBq)
Right frontal	3.75
Left frontal	7.72
Right temporal	4.69
Left temporal	4.69
Cerebellum	4.20

4.3.5 Grid Phantom

A specially designed grid phantom shown in Figure 20 was used to examine the relative quantitative properties of the reprojection correction method.

FIGURE 20 Grid phantom

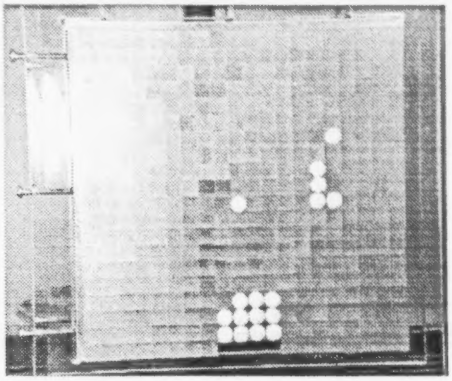

The phantom consists of a 20 x 20 grid of blocks 1 cm x 1 cm x 7 cm in length. Solid perspex, aluminum, and fillable perspex blocks with a 5 mm diameter bore along the length of the block (total volume ~3.5 cc) were used in the phantom.The fillable perspex blocks are the blocks with the white caps in Figure 20. To determine the accuracy of the measured attenuation maps, noise-free digital attenuation maps of the phantom (Figure 21) were also created and compared with the measured ones. Unfortunately, because of the large size of the phantom's support frame, attenuation maps acquired with the line source experienced significant truncation at the corners.

FIGURE 21 Simulated attenuation map of the grid phantom with 4 blocks of aluminum.

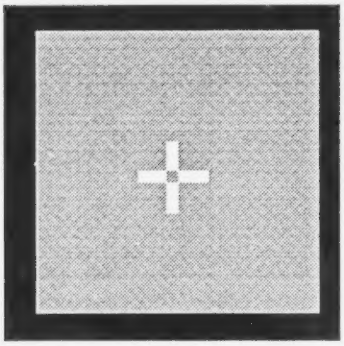

4.4 Acquisition Protocols

To acquire the transmission scans, the line source was filled with between 270-300 MBq of Tc-99m pertechnetate and placed in the holder. The holder was fixed opposite head 1 at the nominal focal length of the fan beam collimators, 50 cm. Ultra-high resolution fan beam collimators were attached to all three heads. For the Jaszczak, uniformity and skull phantoms a rotation radius of 15.5 cm was used. A 18.5 cm rotation radius was used for the grid phantom. A total of 120 projections through 360° were acquired using a 128x128 matrix size for all acquisitions. A 15% energy window centered around the photopeak was used for all acquisitions.

The attenuation coefficients for each object in the linearity phantom were determined by placing the objects on the surface of one of the gamma cameras, and using the line source to measure the transmission through the objects. A blank scan of the line source with no objects was then obtained. The transmission image was converted to attenuation coefficient ray sums by taking the natural log of the ratio of blank scan to the transmission image and then dividing by the thickness of each object to obtain the linear attenuation coefficients. Attenuation coefficients determined in this manner reflect a specific broad beam geometry which may not be applicable to the broad beam geometries used in the transmission scan or the emission scan. However, they should provide a reasonable estimate of the attenuation coefficients for both geometries. Narrow beam attenuation coefficients were obtained for each object from Hubbell [26] and from a CT scan of the phantom, for comparison with the broad beam values.

TABLE 2 Narrow beam attenuation coefficients for the linearity phantom inserts

Insert	Attenuation Coefficient (cm^{-1})	Source
Perspex	0.174	Hubbell
Simulated bone	0.268	Hubbell
Acrylic	n/a	n/a
Aluminum	0.373	Hubbell
White plastic insert	0.290	CT
Clear plastic inset	0.176	CT
Translucent plastic inset	0.142	CT
Water	0.151	Hubbell

Prior to each study, a 128 x 128 planar image of the line source was acquired to provide a reference intensity for the source. The image was acquired for the same amount of time as each projection in the study.

Before to reconstructing the SPECT study and attenuation maps, the projections were preprocessed using a procedure similar to the one described in [24]. The emission data from heads 2 and 3 were added together to improve the count statistics and stored on the system. To remove the emission data from the combined emission and transmission data in head 1, the projections from heads 2 and 3 were averaged together and subtracted from the data obtained from head 1 as shown in Figure 22.

FIGURE 22 Projection preprocessing steps to remove emission data from the combined emission/transmission data in head 1

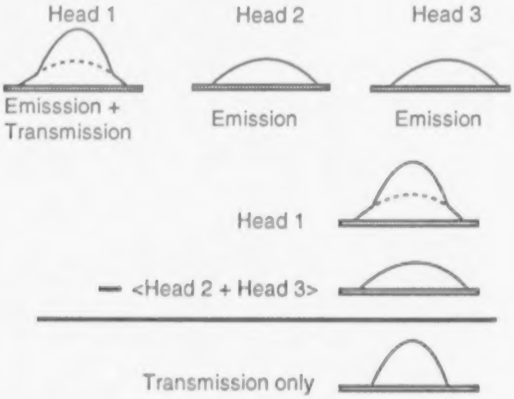

The transmission projections were then converted to linear attenuation coefficient ray sums by dividing each transmission projection into the reference projection and taking the natural logarithm. The results were scaled by

100 to convert the values to integers and stored on the system. Both sets of images were reconstructed at the same time using the reconstruction software provided on the Odyssey computers. This ensures that the same axial emission and attenuation map slices are reconstructed.

For most of the phantom studies, the transmission and emission data were processed using the procedure described in Figure 22. The transmission data were then converted to linear attenuation coefficient ray sums for reconstruction. Prior to reconstructing the linear attenuation coefficients, a low pass filter was applied to smooth the data and reduce the noise level. The low pass filter is described by [64]

$$H(f) = \frac{1}{1 + \left(\frac{f}{f_c}\right)^{2x}} \qquad \text{(EQ 25)}$$

where f_c is the cut-off frequency for the filter and x is the slope or order of the filter. For frequencies above f_c, the low pass filter decreases in amplitude from 1 so that frequencies above f_c are attenuated. In most cases, the cut-off frequency used was slightly lower than the default supplied by the filter program in order to provide some additional smoothing and noise reduction. The order of the filter used remained at the default. For the transmission data, the additional smoothing helped reduce the noise due to statistical variation introduced by the preprocessing (Figure 22) and conversion to linear attenuation coefficients steps.

For the grid and brain phantoms, the emission data were reconstructed and filtered using a 3D Wiener post-filter. The Wiener filter is a resolution recovery filter which adapts to the image being filtered and is generated from the MTF of the imaging system and the object and noise power spectra from the image being filtered. The Wiener filter applied has the form [64]

$$H(f) = \frac{MTF(f)}{MTF(f)^2 + \frac{1}{SNR(f)}} \qquad \text{(EQ 26)}$$

where MTF(f) is the modulation transfer function (MTF) of the system at frequency f and SNR(f) is the ratio of the object power spectrum to the noise power spectrum scaled with a user selectable noise multiplier. In general the shape of the Wiener filter function starts at unity and gradually increases at higher frequencies, then tails off to attenuate high frequency noise. The actual shape of the filter function is dependent on the object and noise power spectra and the system MTF.

The Wiener filter was applied to the reconstructed SPECT images of the phantoms as a three dimensional post-filter. The parameters of the filter used were the default parameters (noise multiplier=0.5) provided by the 3D post-filter program supplied with the Odyssey software. The converted transmission data were pre-filtered with a low-pass filter to reduce the level of high frequency noise introduced by the subtraction operation in Figure 22 and the conversion to linear attenuation coefficients. For all studies, the images were reconstructed using a standard ramp filter.

The Jaszczak phantom was scanned cold and with no water to provide maximum contrast for the visualization of the rods. The line source was filled with 346 MBq of Tc-99m. Data was acquired for 15 s/step, 120 steps over a complete 360° rotation and reconstructed using a standard filtered backprojection routine.

To see how well the reprojection method corrects for a uniform distribution, 246 MBq of Tc-99m was added to the uniform water cylinder. Projections were acquired at 30s/step, 120 steps over 360° and backprojected. The emission projections from heads 2 and 3 were added together, reconstructed and post-filtered using a low pass filter with a cut-off frequency of 0.2 cycles/pixel. The transmission projections were converted to attenuation coefficient ray sums, prefiltered using a low pass filter with a cut-off frequency of 0.2 cycles/pixel and reconstructed.

The acquisition protocol used for the brain phantom was similar to the one used for normal brain SPECT. Ultra-high resolution fan beam collimators (LEUHR-FAN) were mounted on all three heads for the acquisition. Projections were acquired for 10 s/step, 120 steps with an acquisition magnification factor of 1.33. The line source was filled with 263 MBq of activity. Images from the SPECT study were reconstructed and then post-filtered using a Wiener filter. The transmission projections were prefiltered using a low pass filter using a cut-off frequency of 0.2 cycles/pixel and reconstructed.

A simultaneous emission/transmission study of the grid phantom was acquired using ultra-high resolution fan beam collimators (LEUHR-FAN) mounted on all three heads. 120 projections were acquired at 15 s/projection into a 128x128 image matrix step-and-shoot mode with a radius of rotation of 18.5 cm. The line source was filled with 241 MBq of Tc-99m. The SPECT projections were reconstructed and post filtered using a Wiener filter. Two sources were placed in the phantom. The total activity in the sources was 27.3 MBq and 20 MBq. One source was placed at the center of the phantom. The second source was placed above and toward the right of the center source. Three phantom configurations were examined. The first configuration scanned was the phantom with no aluminum blocks present. The second configuration had 2x1 blocks of aluminum placed under and right of the central emission source. The third configuration had two more 2x1 blocks of aluminum placed above and left of the central emission source. The phantom configurations are shown in Figure 23 below.

FIGURE 23 Grid phantom configurations: Dark gray - water filled inserts. Light grey - sources. Black - aluminum blocks. A) No aluminum blocks, B) 2 2x1 aluminum blocks C) 4 2x1 aluminum blocks

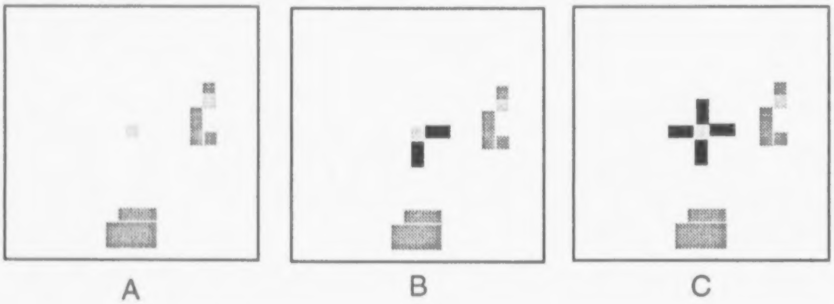

4.5 Attenuation Correction Algorithms

4.5.1 Reprojection algorithm

After the attenuation map and SPECT studies were reconstructed, the reprojection algorithm was applied. The reprojection correction method presented in chapter 3 requires that each pixel in the reconstructed image be multiplied by the exponential of the ray sum of attenuation coefficients from the attenuation map. This requires a complex ray-tracing algorithm in order to compute the intersection length of the projection ray through each pixel (Figure 13) in calculating the attenuation coefficient ray sum. The reprojection method was implemented using a rotating fan beam projection algorithm similar to the technique described in [54]. For simplicity and speed, the projection process was modelled using one dimensional projection rays from the center of each projection bin to the focal point of the collimator. More complex and accurate projection algorithms model each projection as a ray with finite width and/or account for the acceptance angle of the collimator holes. For each projection angle θ, the SPECT image is rotated and projected using a fan beam geometry. A floating point rotation algorithm using a bilinear interpolation algorithm was employed to perform the rotation on the unrotated data to avoid accumulating interpolation errors. A tracing algorithm developed by Siddon [27] was used to determine the length through each pixel intersected by the fan beam projection rays. These intersection lengths were computed prior to projecting the data and stored in memory to speed the process up. 120 projections were calculated through 360°.

The computer implementation of the reprojection method is as follows:

1. Pixel values in the reconstructed attenuation map are converted to linear attenuation coefficients using an experimentally determined linearity relationship.
2. Pixel intersection lengths (d_{ij}) for the fan beam projection rays are calculated.
3. SPECT images are scaled to the number of projections, N.
4. Attenuation map (μ_{ij}) and SPECT study (A_{ij}) are rotated by 3°.
5. For each pixel intersected by the projection ray, $A_{ij} exp\,(d_{ij} \sum_{j} \mu_{ij})$ is computed and added to the projection value p_{ik}.
6. Step 4 repeated until all intersected pixels in the projection ray are done.
7. Advance to the next projection ray, reset p_{ik}, $\sum_{j} \mu_{ij}$ to 0 and repeat Step 4.
8. Advance to the next slice k (k = k + 1) and repeat from Step 2.

4.5.2 Chang algorithm

The effectiveness and validity of the reprojection algorithm was compared with attenuation correction using Chang's algorithm with uniform and non-uniform attenuation maps. For the uniform water phantom, the attenuation correction software supplied with the Odyssey computers was used. The program uses a first order (non-iterated) Chang algorithm assuming uniform attenuation. For the brain and grid phantoms, a program was written to implement the Chang algorithm using the respective non-uniform attenuation maps. 120 projection rays over 360° were used to calculate each element of the correction matrix. The ray tracing method developed by Siddon [27] was used to calculate the intersection length of the ray for each intersected pixel. Again, the projection rays were modeled as one dimensional lines radiating from the center of each pixel outwards. To speed up the implementation of the Chang algorithm, intersection lengths were pre-calculated and stored in memory. Then, for each pixel, the number of intersection points was determined for each ray and the ray sum was computed. The procedure for the non-uniform Chang attenuation correction was as follows:

1. Calculate intersection lengths for 120 rays.
2. Scale SPECT image by the number of projections, N.
3. Calculate the number of intersected pixels for ray m for pixel A_{jk}.
4. For each intersected pixel i, calculate the ray sum $\sum_i \mu_i \Delta x_i$ where Δx_i is the pixel intersection length. Calculate $exp(-\sum_i \mu_i \Delta x_i)$ for this ray and add to $\sum_m exp(-\sum_i \mu_i \Delta x_i)$.
5. Go to next ray m = m + 1 and go back to Step 3.

6. The correction matrix element for pixel A_{jk} is

$$C_{jk} = \frac{M}{\sum_m exp\,(-\sum_i \mu_i \Delta x_i)} \quad .$$

7. Go to the next pixel in A_{jk} and repeat from Step 3.

8. Calculate the corrected image, $A'_{jk} = A_{jk} C_{jk}$.

CHAPTER 5

Results and Discussion

5.1 Attenuation Map

5.1.1 Linearity

All of the objects used in the linearity phantom (Figure 17) were placed on the surface of head 1 and a planar image of the photon transmission was obtained using the line source to illuminate the objects. A second image was obtained with no objects in the gamma camera field of view. This image was used to provide the reference intensity of the line source, I_0. The ratio of the two images was calculated, and the natural log of the result was taken so that the value of each pixel represented the total attenuation coefficient through the object, $\mu x = ln(\frac{I_o}{I})$. An ROI was drawn over the center of each object to obtain the average pixel value of the object. This was divided by the thickness of the object, x in cm, to determine the attenuation coefficient for the object.

Table 3 below gives the attenuation coefficients obtained for each object in the linearity phantom. Attenuation coefficients for each object determined from a CT scan or from Hubbell [26] are supplied for comparison where available. The experimentally determined attenuation coefficients will generally be lower than the narrow beam values due to the inclusion of scatter events.

TABLE 3 Attenuation coefficients for linearity phantom objects

Object	Thickness (cm) (±0.05 cm)	Experimental attenuation coefficient (cm^{-1})	Narrow beam attenuation coefficient (cm^{-1})
Perspex blocks	2.0	0.155±0.060	0.178
Simulated bone	2.8	0.246±0.048	0.278
Aluminum blocks	2.0	0.365±0.073	0.390
White plastic insert	3.8	0.268±0.035	0.290
Acrylic	2.8	0.175±0.039	-
Translucent plastic insert	3.8	0.116±0.030	0.142
Water	4.5	0.149±0.028	0.155

The uncertainties in the attenuation coefficient calculation were determined using standard error analysis and error propagation techniques [28] applied to Equation 14. Uncertainties were calculated from the equation

$$\delta\mu = |\mu| \sqrt{\left(\frac{\delta x}{x}\right)^2 + \left(\frac{\sqrt{\frac{1}{I_o} + \frac{1}{I}}}{\ln\left(\frac{I_o}{I}\right)}\right)^2} \qquad \text{(EQ 27)}$$

Narrow beam linear attenuation coefficients for the white and translucent plastic inserts were obtained from an x-ray CT scan. For the perspex, aluminum, bone and water inserts, the narrow beam attenuation coefficients were obtained from Hubbell [26].

A gamma ray CT study was then obtained of the phantom using the line source. 120 projections were obtained over 360° for 15 seconds/projection. Projection data was acquired in 128 x 128 pixel matrices. Two images were reconstructed with a ramp filter and analyzed; one slice through the center of the inserts excluding the water bag and a second slice including the water bag but excluding the three plastic inserts. No additional filtering was performed. Each slice was 3.56 mm thick. The reconstructed slices are shown in Figure 24 below. The layout of the objects is described in Figure 17.

FIGURE 24 Transmission images of the linearity phantom. Left) through the phantom base. Right) through the water bag.

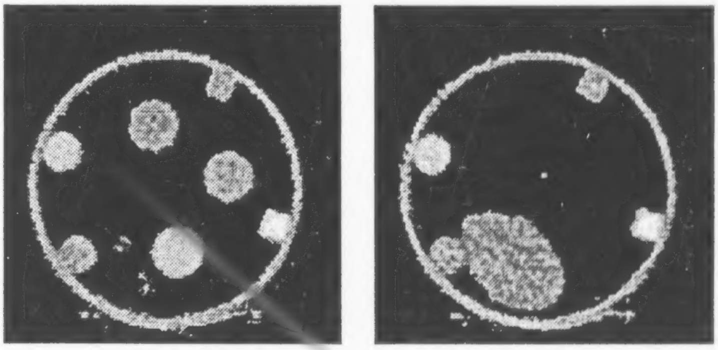

ROIs placed over each object were used to obtain a mean pixel value for each object. The information from the ROIs is summarized in Table 4 below.

TABLE 4 ROI data from the linearity phantom.

Object	Mean pixel value	Total Counts	Total Pixels
Simulated bone	902.5	35194	39
Translucent plastic	469	77682	135
Perspex blocks	517.5	23973.5	46
Clear plastic insert	582	78552	135
Acrylic	575.5	22443	39
Water bag	490	273818	559
White plastic inset	918	15988	135
Aluminum blocks	1242	60862.5	49

The mean pixel value from the ROI for each object was plotted against the attenuation coefficients in column 3 of Table 3. A linear regression analysis was performed using Mathematica's Linear Regression package to determine an equation correlating the pixel values in the attenuation map to linear attenuation coefficients, yielding

$$\mu = (2.90\times10^{-4} \pm 1.16\times10^{-5})\,x - (1.49\times10^{-3} \pm 8.48\times10^{-3}) \qquad \text{(EQ 28)}$$

with $R^2 = 0.9905$, where x is the pixel value from the reconstructed image, and μ is the attenuation coefficient in cm^{-1}. This equation will be used to convert the pixel values of the reconstructed attenuation maps to linear attenuation coefficients for use in the reprojection method. A graph of the linear attenuation coefficients as a function of the pixel value is shown in Figure 25 below.

The solid line indicates the line of best fit determined from the regression analysis, and the points indicate the data points.

FIGURE 25 Plot of linear attenuation coefficients vs. reconstructed pixel value. Points are the ROI data. The solid line represents Equation 28

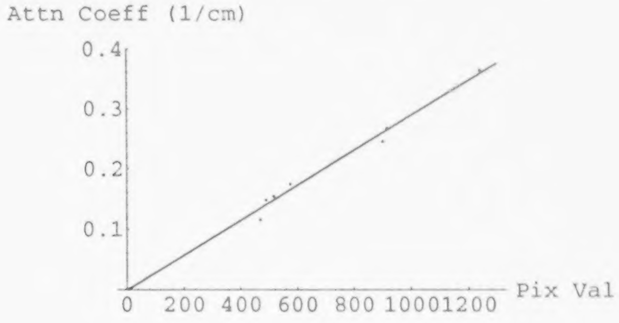

5.1.2 Resolution

Figure 26 shows a 3.56 mm thick slice reconstructed through the center of the rod section of a Jaszczak phantom. The image was reconstructed with no additional filtering applied. Each wedge of rods is clearly visible, demonstrating that the transmission scans are capable of producing high contrast-resolution images with a resolution of at least 6.4 mm. Underneath the phantom, some of the headrest can be made out. The phantom contains no water to maximize the contrast of the rods. It should be noted however, that since there is no water in the phantom, and therefore little scatter, this is a somewhat optimistic estimate of the resolution of the transmission scans. The actual high contrast resolution for the transmission source setup is expected to be lower due to scatter.

FIGURE 26 Attenuation map of the rods in the Jaszczak phantom.

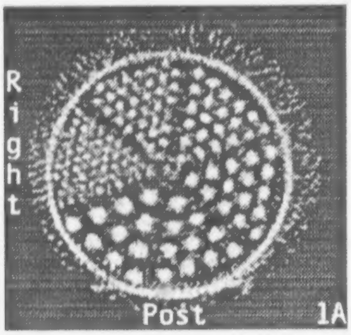

5.2 Digital Simulations

The reprojection method developed in Chapter 3 was tested using simulated SPECT and attenuation map data modelling the grid phantom. A series of 7 simulated SPECT images, each consisting of a single square source positioned from the top right corner of the grid phantom to the bottom left corner, were corrected for attenuation with the reprojection method using a simulated attenuation map and reconstructed. Figure 27 shows the series of simulated data.

FIGURE 27 Simulated SPECT data for the grid phantom.

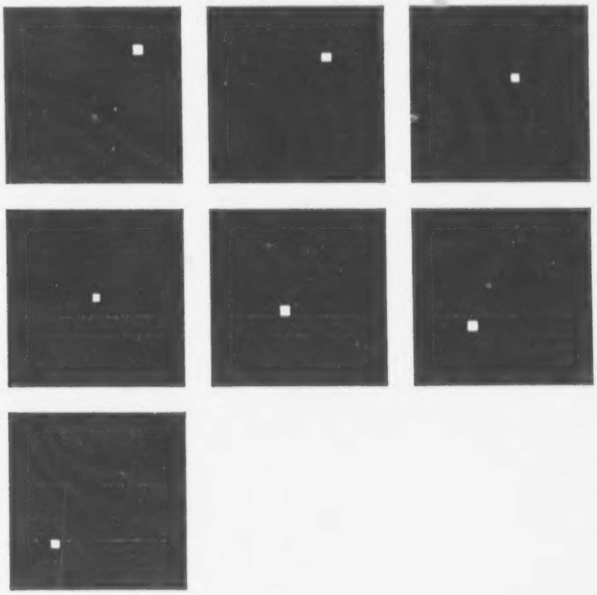

The variations in source size in Figure 27 are due to floating point round-off error when the images are generated.

The simulated attenuation map that was applied modelled a uniform grid phantom composed entirely of perspex grid blocks. The corrected images are shown in Figure 28 below.

FIGURE 28 Attenuation correction of simulated SPECT images.

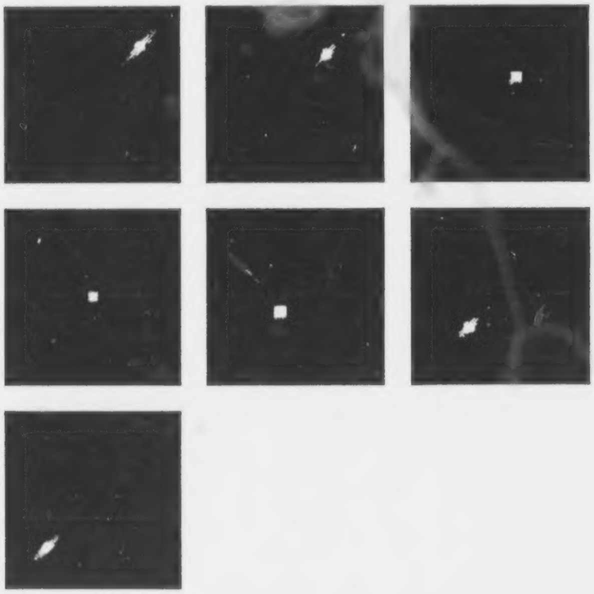

The source of the blurring was thought to be due to the simple assumptions made in the forward projection process, and due in part to the ramp filter applied in the backprojection. Currently, the projection algorithm uses a simple ray-driven approach without considering collimator and detector effects. More accurate modelling of the projection process should reduce the amount of blurring that occurs. A method is described by Zeng et al [29] where the detector response is measured at various heights above the detector and used to derive a detector response function (DRF). For each layer of voxels in the image volume parallel to the detector (in each layer the voxels will be a fixed distance above the detector plane), the Fourier transform of the layer is computed and multiplied with the Fourier transform of the DRF. Then the inverse Fourier transform is applied and the result is used to calculate the contribution of the layer to the projections.

Another source of the blurring is likely the ramp filter employed in the filtered backprojection. In the frequency domain, the response of the ramp filter increases linearly with frequency up to a certain cut-off frequency. Because of the finite cut-off frequency (usually 1/2a where a is the image pixel dimension) of the ramp filter, high frequency components above the cut-off frequency are not preserved. In the frequency domain, sharp edges are represented by the high frequency component and since the ramp filter has a finite cut-off frequency, this means that some of the high frequency components that make up the sharp edges of the simulated source will be lost, causing the blurring.

There is also a slight distortion of the simulated source at the corners where the source is near the edge of the field of view. Because of the proximity to the edge of the reconstruction FOV, there may be some projections where the source is outside the fan beam field of view. Reconstructing the source with the source missing in some projections may have caused the distortion in the reconstructed images. Since the source will be well within the reconstruction field of view in almost all cases, this is a relatively small concern.

Figure 29 is a line profile through the simulated source at the center of the phantom with the counts in both profiles normalized to 1.

FIGURE 29 Line profiles through the simulated source at the center of the phantom. Counts normalized to 1.

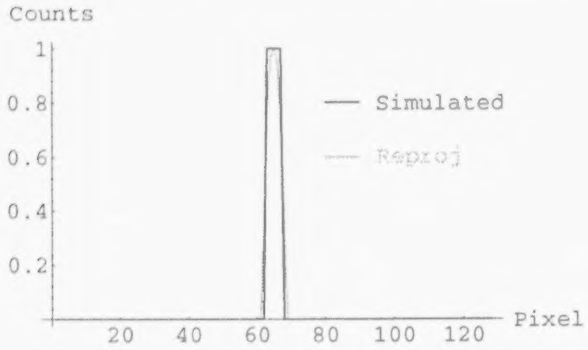

The extent of blurring is easily seen. The actual amount of blurring is very small, only a few pixels on either side of the source.

5.3 SPECT Sensitivity

In order to perform some simple quantitative analysis on the phantom studies to evaluate the potential of the reprojection algorithm, a technique was required to correlate the pixel values in the reconstructed images to an absolute activity concentration. SPECT sensitivity for quantitation purposes was determined using 5 film cannisters filled with different activity concentrations. For each source, a small amount of activity was injected into 25 cc of water. The total activity in each source was measured and divided by the volume of water to get an activity concentration, summarized in Table 5 below.

TABLE 5 SPECT sensitivity source concentrations.

Source	Injected Activity (MBq) (±0.1 MBq)	Activity Concentration (MBq/cc)
1	29.4	1.176±0.005
2	62.4	2.496±0.006
3	50.3	2.012±0.006
4	36.2	1.448±0.005
5	80.8	3.232±0.005

The uncertainty in activity concentration was determined using standard error analysis techniques [28].

Ultra high resolution fan beam collimators (LEUHR-FAN) were mounted on each head to perform a SPECT study on the containers. A triple head SPECT acquisition of the sources was performed using 128 x 128 pixel acquisition matrices and 120 projections at 10, 20 and 30 seconds/projection in continuous scan mode.

For each source, a SPECT image was reconstructed and 3D post filtered with a Wiener filter. The parameters of the Wiener filter used were the default settings provided by the 3D postfiltering program supplied on the Odyssey computer. An 8 x 14 pixel ROI was drawn around each source enclosing an area containing counts greater than 80% of the maximum pixel value. From each ROI, a mean pixel value was obtained. The results are summarized in Table 6 below.

TABLE 6 ROI counts

Source	Mean ROI Counts (10s)	Mean ROI Counts (20s)	Mean ROI Counts (30s)	Average ROI cps
1	2247	4198	6423	216±11
2	4561	8432	11777	423±15
3	3779	7252	10275	361±14
4	2708	4790	6915	547±11
5	5913	11282	16037	563±17

As can be seen from the table, the counts in each ROI scale linearly with the acquisition time. To remove this time dependence, the ROI counts were normalized to acquisition time by dividing by the acquisition time per projection step. The last column, Average ROI cps, is the average of the time normalized counts from columns 2, 3, and 4. The average count rates were plotted against the actual activity concentration in Table 5 to determine a linear relation correlating activity concentration to the reconstructed pixel value (Figure 30).

FIGURE 30 Relationship between source activity concentration and pixel counts/second.

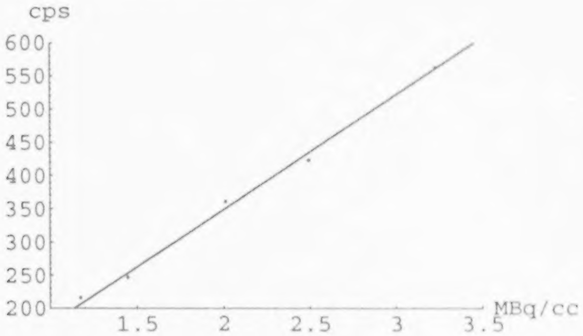

The solid line indicates the line of best fit determined from the regression analysis and the dots indicate the data points from Table 5 and Table 6. The equation of the solid line was determined using linear regression analysis:

$$y = (172.60 \pm 3.86)x + (3.68 \pm 7.76) \quad \text{(EQ 29)}$$

with $R^2 = 0.998$, where x is the activity concentration in MBq/cc and y is the corresponding pixel value in counts/second. This equation can be easily inverted to provide the activity concentration as a function of the pixel value in counts/second,

$$x = (0.00576 \pm 0.00013)y - (0.018 \pm 0.045) \quad \text{(EQ 30)}$$

The uncertainties in the regression coefficients of Equation 30 were determined by the analysis software.[1] Equation 30 will be used later to perform a simple quantitative analysis of both the Chang and reprojection methods for the phantom studies. The pixel values of the reconstructed SPECT images are divided by the acquisition time/step, and converted to an activity concentration by Equation 30. Assuming that the entire acquisition/reconstruction/filtering chain is a linear system, this simple quantification technique should provide accurate activity concentrations from the pixel values in the reconstructed images.

---

[1] Mathematica (Wolfram Research, Inc.) Linear Regression package

5.4 Uniform Water Phantom

Figure 31 below shows a SPECT slice of the uniform water phantom from a simultaneous emission/transmission study. The image was reconstructed and post filtered using a low pass filter with a cut off frequency of 0.2 cycles/pixel.

FIGURE 31 Reconstructed slice from a SPECT study.

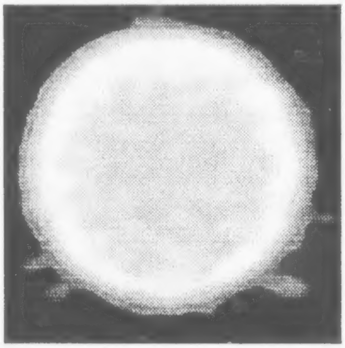

Figure 32 below shows a line profile through the center of the phantom showing the decrease in counts towards the center due to attenuation. The decrease in counts is about 50% of the counts in the outer rim of the phantom.

Because of scatter, the count density in the central region is higher than it would be for photon attenuation alone.

FIGURE 32 Line profile through the center of Figure 31.

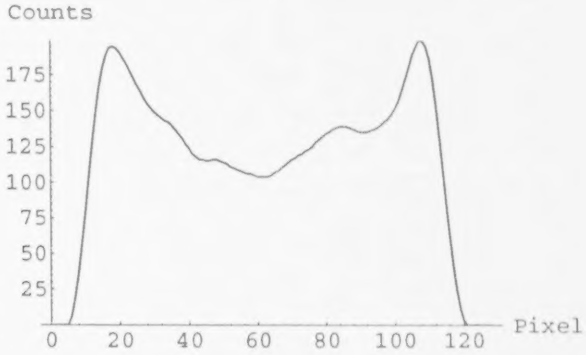

The corresponding attenuation map for the uniform water phantom is shown in Figure 33 below. The transmission projections were converted to attenuation coefficient ray sums, and the resulting projections prefiltered using a low pass filter with a cut off frequency of 0.2 cycles/pixel (to reduce the level of noise in the projections) and reconstructed.

FIGURE 33 Attenuation map of the uniform water phantom.

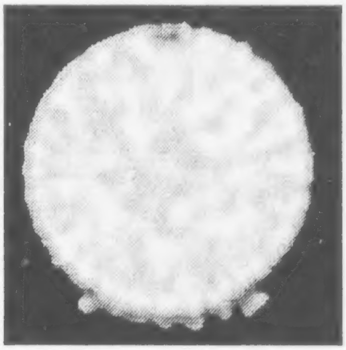

Part of the head rest can be distinguished in the bottom portion of the image, and an air bubble in the phantom can be seen at the top. The attenuation map appears fairly flat, as expected for a uniform attenuation distribution, although somewhat noisy. A line profile taken through the center of the attenuation map showing the attenuation coefficients in cm^{-1} is shown in Figure 34.

FIGURE 34 Line profile through the center of Figure 33.

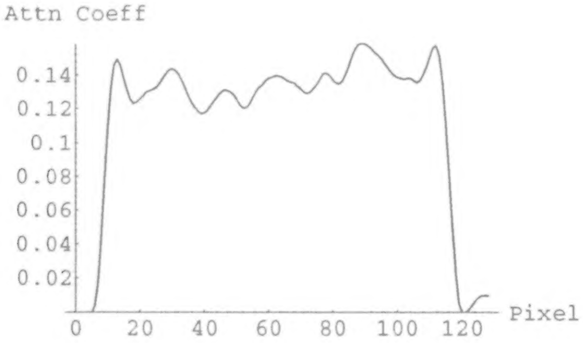

An examination of the line profile shows that the attenuation coefficients in the water phantom are slightly underestimated, with the mean attenuation coefficient in the profile around 0.13 cm^{-1} rather than $\mu=0.149$ cm^{-1} as determined from the linearity phantom for water. The apparent decrease in attenuation coefficient is likely due to a high number of detected scatter events from both the emission and transmission sources in the transmission data. The additional scatter contribution from the emission source will cause some problems with performing accurate attenuation compensation by increasing the apparent photon transmission in head 1 (the transmission head) and therefore lowering the effective attenuation coefficients in the attenuation maps. The attenuation coefficients in Table 3 and the linearity relationship derived previously (Equation 28) included only scatter events from the transmission source. Additional scatter will alter the linearity relationship slightly so that Equation 28 will underestimate the actual attenuation coefficients. In the case of the attenuation map above, there is an additional scatter contribution from the activity in the water phantom itself. These additional scattered photons detected in head 1 will cause a slight increase in the number of detected counts, and therefore result in a further decrease in the linear attenuation coefficient. There is also considerable inter-slice crosstalk due to the lack of line source collimation in the axial direction, illustrated in Figure 35.

FIGURE 35 Side view of line source-detector arrangement showing inter-slice crosstalk events.

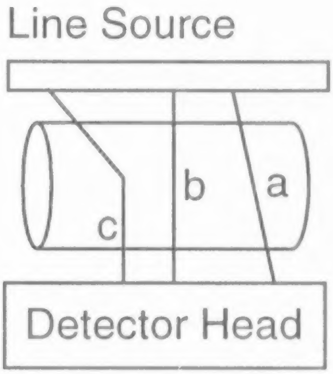

Figure 35 illustrates 3 types of cross-plane events involving photopeak photons (these can also be classified as scatter events). Event a shows an unscattered photopeak photon emitted from one section of the line source which has been detected in a different slice than the photon was emitted from. Event b shows a photon detected in the same slice, and event c shows an example of singly or multiply scattered photon detected in a different slice than it was emitted from. This problem can be easily solved by modifying the line source holder to include source collimation in the axial direction and has been shown to produce extremely high quality attenuation maps [30]. Simulations and phantom studies performed by Cao and Tsui [61] and Kemp et al. [30] have shown that with a properly designed source collimator, the resolution of the transmission system is determined by the resolution of the source collimator rather than the detector collimator. In particular, the resolution of the transmission imaging system is determined by the collimator with the higher resolution. The trade-off with using a source collimator is decreased detection efficiency, although this can be compensated for by increasing the source activity so that the photon flux from the collimated source is comparable to the uncollimated source.

The SPECT image in Figure 31 was corrected for attenuation using the reprojection method developed in Chapter 3 with attenuation coefficients obtained from the attenuation map in Figure 33. A total of 120 projections through 360° at 3° increments were generated and then reconstructed. The result is shown in Figure 36.

FIGURE 36 Attenuation corrected SPECT image of Figure 31 using the reprojection method.

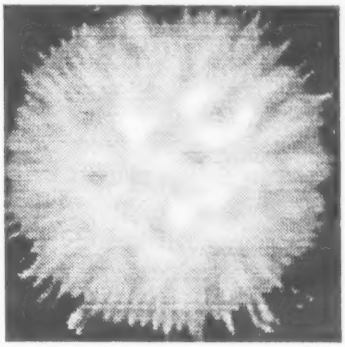

The reprojection method does compensate for the loss of counts in the center of the phantom due to attenuation. An unfortunate and noticeable aspect of the attenuation corrected image is the high degree of nonuniformity in the image. There is a decrease in activity towards the periphery and increased activity in the center. The corrected images are quite mottled and not very uniform. Radial lines around the edge of the phantom can be seen, and are probably due to the digital projection process.

The over correction in the center is due to the fact that in the central regions, the attenuation length ($exp(\sum_{j'} \mu_{ij'} d_{ij'})$ in Equation 24) will have the greatest magnitude for pixels far away from the detector, and thus will provide the greatest weighting factor to the projection of each pixel. The relative contribution at the edges of the projection volume is lower as well. At the edges of the projection volume, the amount of attenuating medium is low, and there are fewer emitting pixels intersected by the projection rays, so the contribution of the periphery of the phantom is lower compared to the center of the projection.

Figure 37 shows a line profile through the center of Figure 36.

FIGURE 37 Line profile through the center of Figure 36.

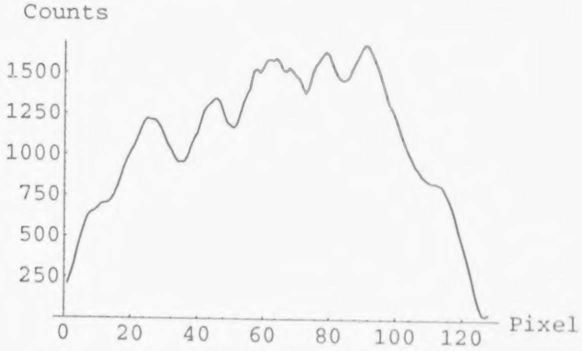

Closer examination of the attenuation map (Figure 33) and Figure 36 reveals noise patterns in the attenuation map that are greatly enhanced in the corrected SPECT image. The noise is primarily statistical in nature. A horseshoe shaped structure in the upper right quadrant of the corrected image can also be seen in the attenuation map. The noise in the attenuation map appears to have been enhanced and amplified in the corrected image.

One of the reasons for this is likely the exponential weighting factor introduced by the attenuation correction. Looking at Equation 24 on page 43, the contribution of each pixel in the reconstructed SPECT image, C_{ij}, is weighted with the exponential of the summation over μ_{ij}. The summation $\sum_j \mu_{ij} d_j$ incorporates the noise along the projection ray. The exponential of the sum greatly amplifies the noise in the projection calculation. The result is that the noise in the attenuation map is amplified and incorporated into the attenuation correction.

For comparison, the uniform water phantom was corrected for attenuation using the attenuation correction routine supplied on the Picker Odyssey workstations. The routine implements a uniform Chang correction algorithm using an attenuation specified by the user. An attenuation coefficient of μ=0.149 cm^{-1} was used. The corrected image is shown in Figure 38.

FIGURE 38 Attenuation correction of the uniform water phantom using the Chang method.

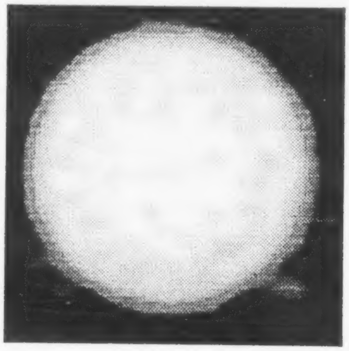

The Chang corrected image is considerably more uniform than the original SPECT image and the reprojection image, although there is a slight over correction in the center. The overcorrection occurs because the attenuation coefficient used (μ=0.149 cm^{-1}) was higher than what would normally be used. In practice, because of the additional events due to scatter, a lower effective attenuation coefficient (typically μ=0.12 cm^{-1}) is usually used with the Chang algorithm in order to account for scatter. Figure 39 shows a line profile through the center of the Chang corrected image.

FIGURE 39 Line profile through the center of Figure 38.

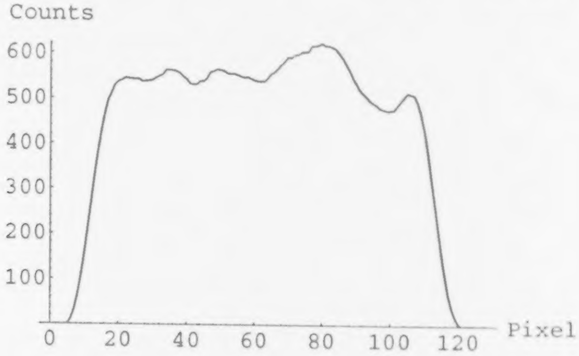

The count level has been increased dramatically by the uniform Chang method compared with the original SPECT image.

Figure 40 shows line profiles through the center of the phantom after the pixel values have been converted to an activity concentration using Equation 30. The activity concentration in the phantom was 0.036 MBq/cc and is indicated on the graph by the solid horizontal line.

FIGURE 40 Quantitative analysis of the water phantom.

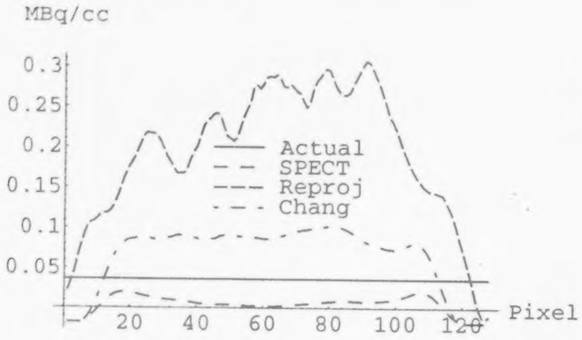

The negative values in the plot above are an artifact as a result of the negative intercept in Equation 30. Both the Chang and reprojection method have greatly overcorrected the activity concentration in the phantom, although the Chang comes closer to the actual activity concentration than the reprojection method, and is considerably more uniform. Whether or not the projection algorithm used to compute the attenuation corrected projections is quantitative is unknown as yet. Since the assumptions made by the projection process are somewhat simplistic compared to the real life case, the simple quantitative analysis performed here and on the remaining phantom studies should be taken lightly. The uniformity problems experienced with the reprojection method suggest that it may not be suitable for large extended activity distributions. Such a limitation would certainly affect the application of this method to brain imaging.

5.5 Brain Phantom

Figure 41 below shows a series of 25 2.67 mm thick SPECT slices from a simultaneous emission/transmission scan of the brain phantom. The SPECT images were reconstructed and post filtered with a Wiener filter. The images below are oriented with anterior towards the bottom of each image and sliced superior to inferior. The two frontal lobe inserts are at the bottom and the cerebellum insert is at the top. The left side of the brain is on the right side of each image, so the images are arranged as if the skull was placed face down and the viewer looking from the top of the skull. A full range gray scale (0 - 100%) was used for Figure 41.

FIGURE 41 Reconstructed SPECT slices from the brain phantom.

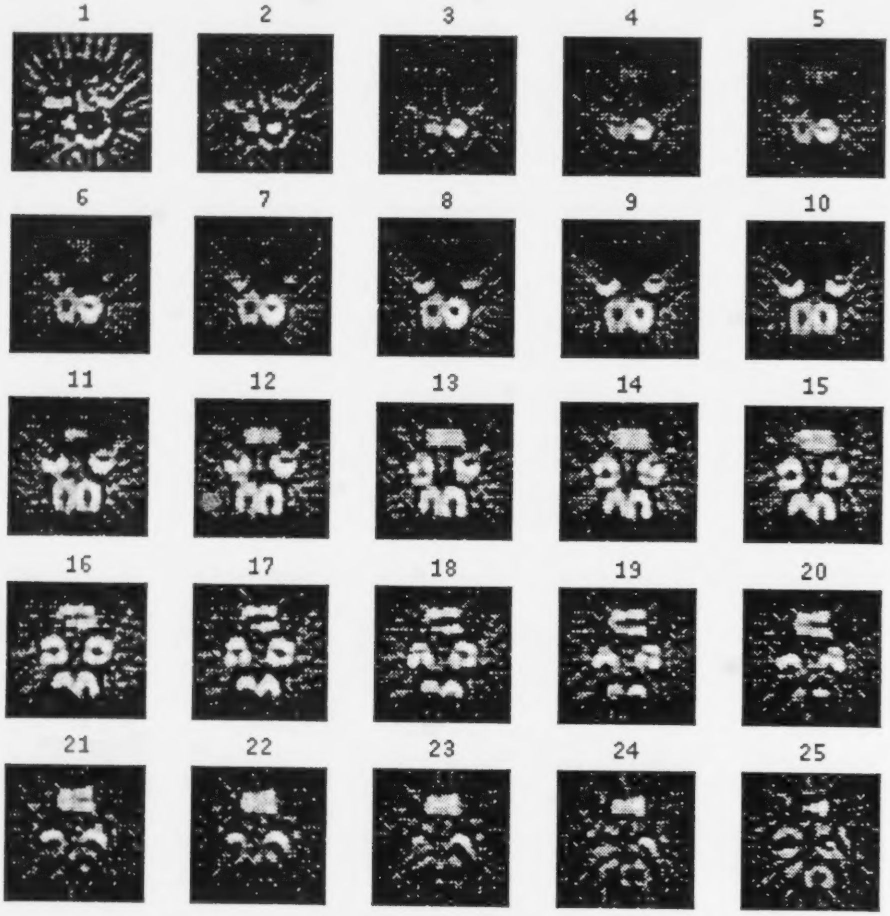

The cold spots in each of the brain phantom inserts are caused by the nylon plastic inserts in each film cannister.

The corresponding attenuation maps are shown below in Figure 42. The transmission projections were prefiltered using a low-pass filter with a 0.2 cycle/pixel cut-off frequency and reconstructed.

FIGURE 42 Attenuation maps of the brain phantom.

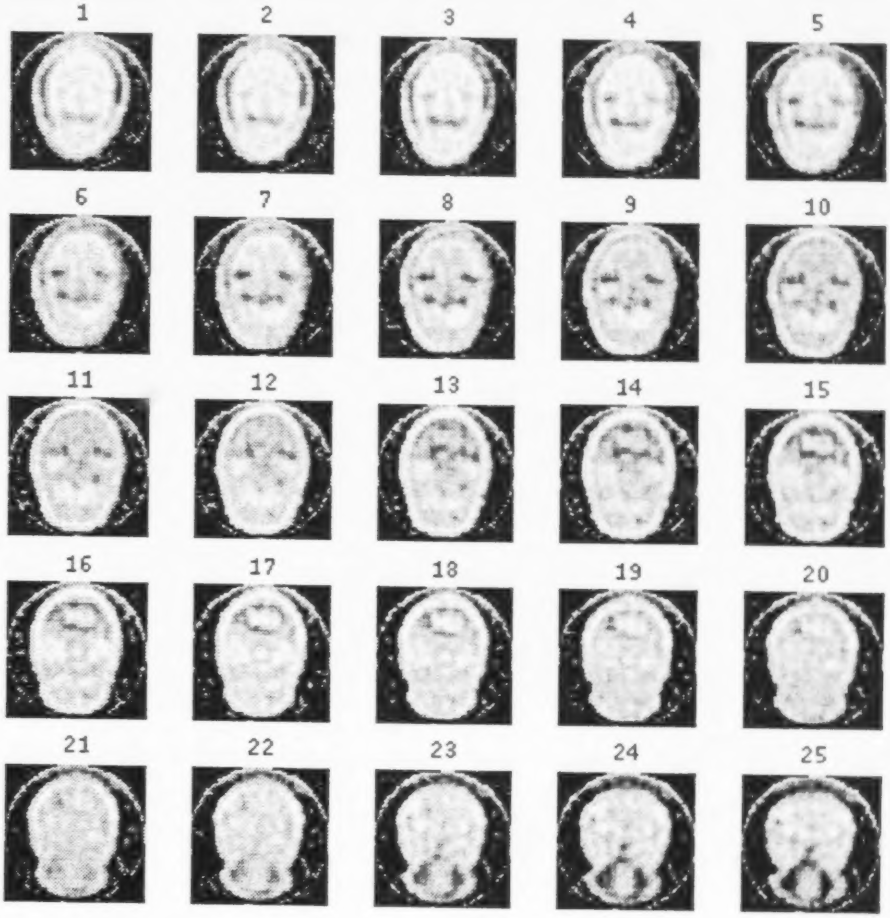
1
2
3
4
5
6
7
8
9
10
11
12
13
14
15
16
17
18
19
20
21
22
23
24
25

The dark low intensity regions in the attenuation maps are air spaces between the wax, skull and hot inserts. There is good contrast between the paraffin/beeswax mixture and the skull.

Figure 43 shows the SPECT images corrected using the reprojection algorithm.

FIGURE 43 Reprojection corrected brain phantom images.

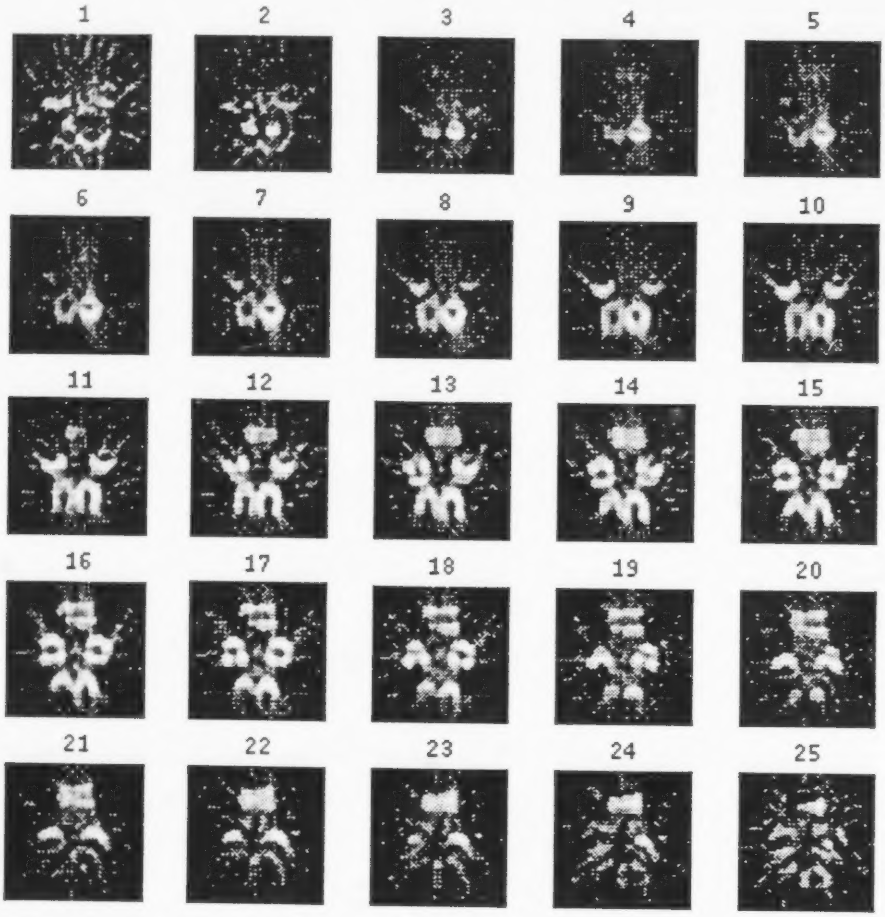

The images corrected with the reprojection method are slightly blurrier than the original SPECT images. There is some streaking apparent, and the frontal lobe inserts in images 13-16 appear more flared than the corresponding images in Figure 41. Much of the background around the inserts seems to have been removed though.

The Chang corrected SPECT images are show in Figure 44.

FIGURE 44 Chang corrected brain phantom images.

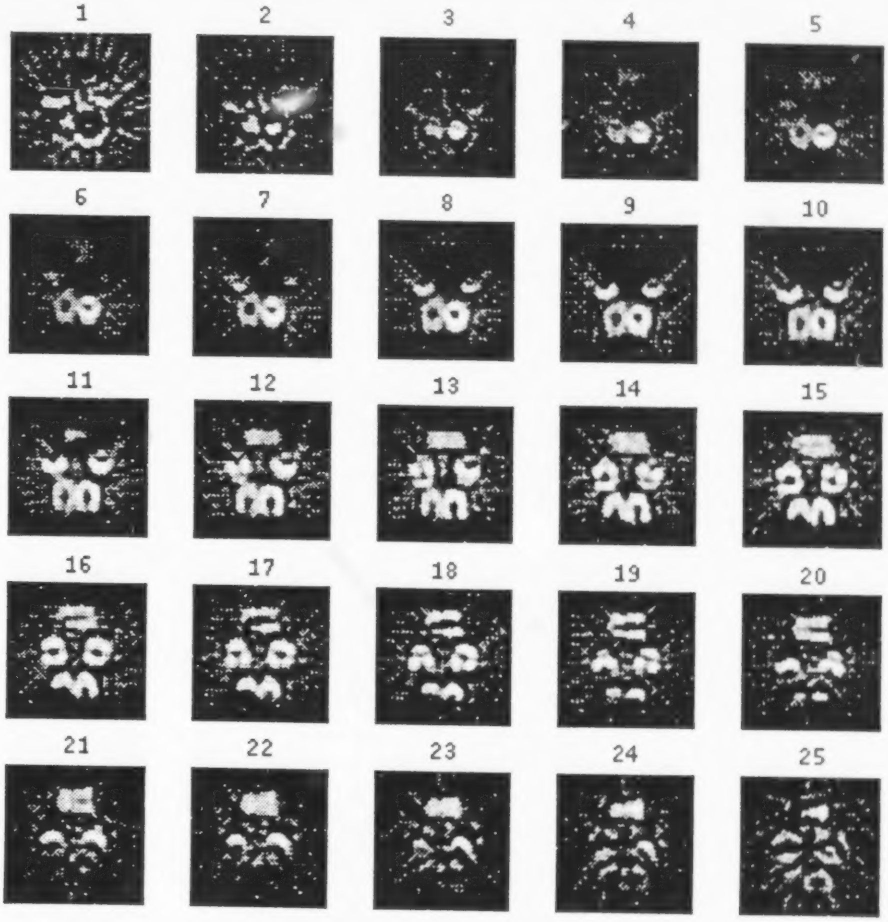
1
2
3
4
5
6
7
8
9
10
11
12
13
14
15
16
17
18
19
20
21
22
23
24
25

The Chang corrected images look almost identical to the original SPECT images. The noise around the edges of the phantom is slightly reduced.

Figure 45 shows a single slice (slice 9) illustrating the results of each attenuation correction method using a full range gray scale (0-100%). The images are in the same orientation as Figure 41.

FIGURE 45 Slice 9 from the original SPECT, reprojection and Chang corrected images.

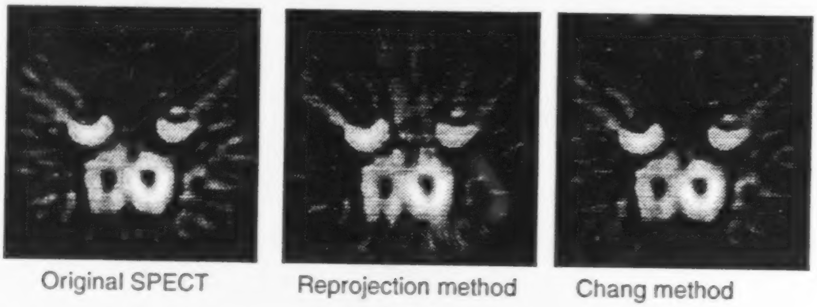
Original SPECT Reprojection method Chang method

Both the Chang and reprojection method have increased the signal to noise ratio, which is evident in the decreased background around the phantom. However, the reprojection method shows some anomalous streaking artifacts which radiate from the right frontal lobe insert. This streaking may be related to the radial lines seen in the images of the uniform water phantom corrected using the reprojection method. It is interesting to note that the streaking appears to radiate from the hotter frontal lobe source. This suggests that the streaking may also be related to an overcorrection when those pixels in the hotter source are projected. In the reconstruction, the backprojection process smears the filtered projection data over the entire image matrix, so that pixels that normally contain no counts have a non-zero value. Normally, this is compensated for by the negative lobes of the filtered projections at other angles.

Consider the correction of projections when the hotter source is furthest away from the detector. In this position, the amount of tissue between the source and the detector is greatest, and therefore when the correction is applied, each of the projected pixels will receive a large exponential weighting. At other projection angles, the attenuating thickness is considerably smaller, so the projections in those directions will receive a smaller weighting.

Now backproject the corrected projections. The overcorrected projections will provide a large contribution to the backprojected image along their respective projection rays compared to the contribution from other projection angles. If the negative lobes of the filtered projections at the remaining angles are insufficient to compensate for this, then the residual might appear as streaking along the direction where the correction was greatest.

The attenuation map corresponding to the SPECT images in Figure 45 is shown below with the same orientation as the images above.

FIGURE 46 Attenuation map for Figure 45.

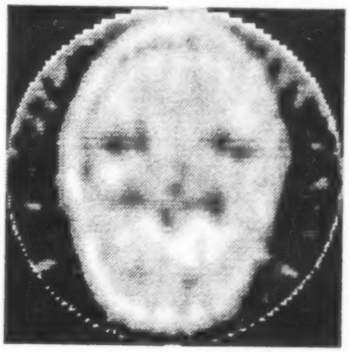

The dark low density regions within the brain are caused by air gaps between the inserts and the brain. The background noise around the edges of the FOV in Figure 46 is probably scatter from the table and non-uniformities at the very edges of the transmission scans. Figure 47 shows a line profile through the middle of the frontal lobe inserts in Figure 45.

FIGURE 47 Line profile through the frontal lobe inserts of Figure 45.

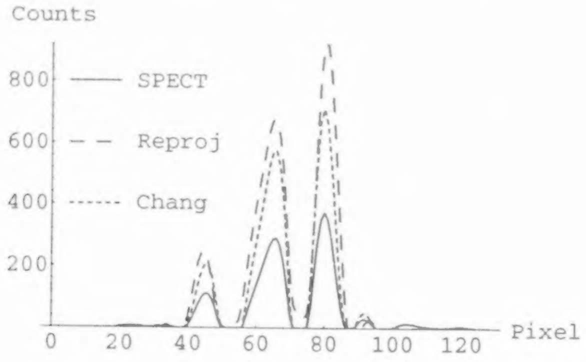

There is a large increase in the count levels seen in both the Chang and reprojection methods.

A single slice taken at a slightly lower level showing the cerebellum insert is shown below in Figure 48.

FIGURE 48 Slice 14 of the brain phantom

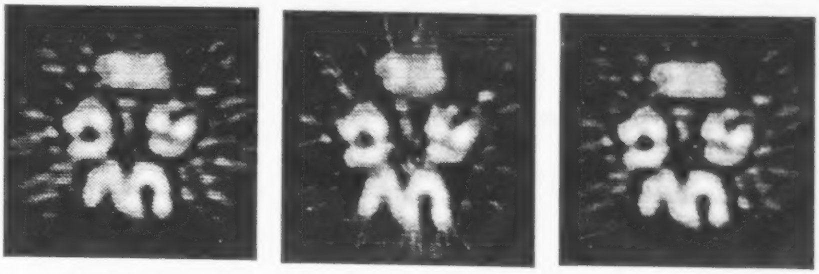

Original SPECT Reprojection Method Chang Method

The background in the middle image has been mostly removed, although there is some noticable streaking in the vertical direction. Also, the right temporal lobe inset (left side of the image) in the reprojection image appears to have been filled in slightly. Both temporal lobe sources appear to be slightly distorted in shape and seem to have been connected to the frontal lobe sources as well. Both the reprojection and Chang method show increased signal to noise, although the reprojection method has some noticeable streaking in the vertical direction.

The corresponding attenuation map is shown below.

FIGURE 49 Attenuation map corresponding to the SPECT slices in Figure 48.

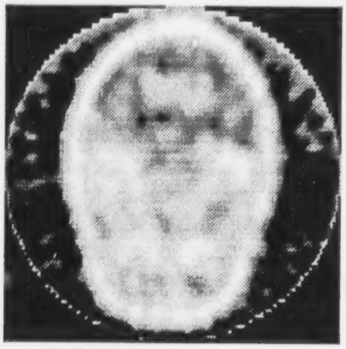

The low density region towards the back of the brain (top of the image) is due to the interface between the inserts and the two portions of the beeswax/paraffin "brain".

Figure 50 shows a line profile through the center of the frontal lobe inserts of Figure 48 obtained at the same level as the line profile in Figure 47. In this graph, the profile line passes through the frontal lobe inserts just above the center of the inserts, about through the center of the ring of activity of the insert.

FIGURE 50 Line profile through the frontal lobe inserts in Figure 48.

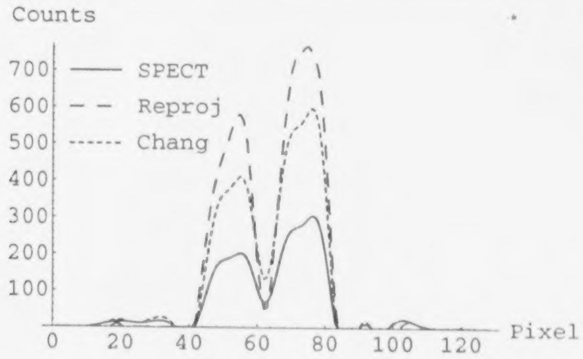

The line profile shows significantly increased counts in both the reprojection and Chang methods.

5.5.1 Brain Phantom Quantitation

Figure 51 shows the activity concentration in the profile from Figure 47 after conversion using Equation 30.

FIGURE 51 Quantitative analysis of the brain phantom.

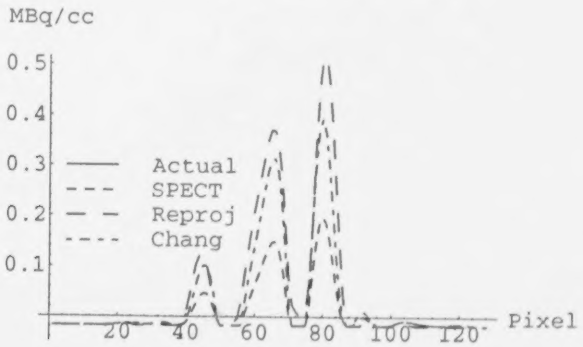

As with the uniform water phantom, the negative values in the graph above are an artifact caused by the negative intercept in Equation 30. The actual activity in each source was 1.5 MBq/cc and is not shown on the graph. One of the problems observed with the inserts was some water leakage out of the inserts, so this could be partly responsible for the poor quantitation results. All three methods have significantly underestimated the activity concentration. Both the reprojection and Chang method show improved relative quantification and increased contrast between hot and cold areas. Additional work will need to be performed to investigate the cause for the underestimation. Future phantom studies with a more realistic brain phantom are planned.

5.6 Grid Phantom

Figure 52 below shows 3.56 mm thick SPECT slice from a simultaneous emission/transmission study of the grid phantom with 0, 2 and 4 aluminum inserts placed around the central hot source.

FIGURE 52 SPECT slices through the middle of the grid phantom.

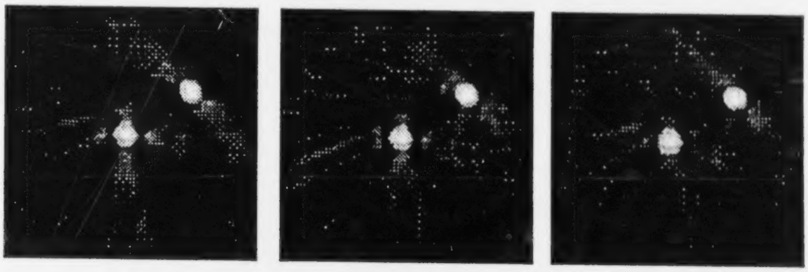

No Aluminum 2 Aluminum blocks 4 Aluminum blocks

The background streaking was thought to be a result of the discrete angular sampling in the acquisition. Figure 53 shows profiles through the central source showing the effect of aluminum on the reconstructed intensity of the central source.

FIGURE 53 Line profiles through the central source of the grid phantom with 0, 2 and 4 aluminum inserts.

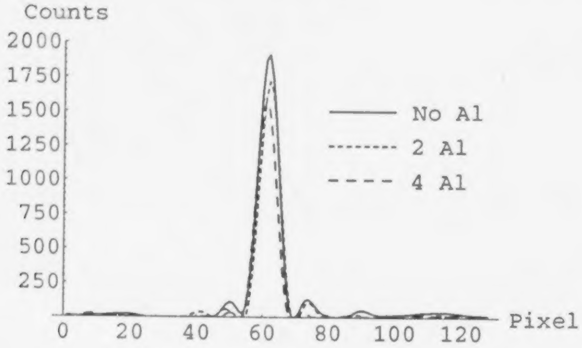

The presence of four aluminum blocks around the central source has resulted in a 17.5% decrease in reconstructed source activity compared to the configuration with no aluminum around the central source.

The corresponding attenuation map from the simultaneous emission/ transmission study for the case of no aluminum blocks is shown in Figure 54 below.

FIGURE 54 Attenuation map with no aluminum blocks.

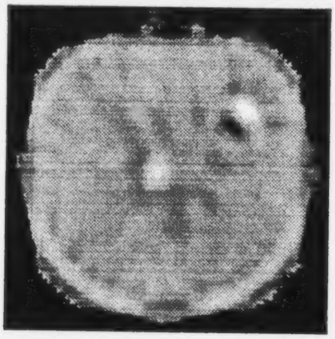

One of the more noticeable features of the attenuation map is the truncation of the corners of the phantom. This is a result of the transmission projections being truncated by the short focal length of the collimators. Truncation of the transmission study is highly undesirable as it can cause artifacts in the reconstructed attenuation map. However, reconstruction algorithms such as ML-EM methods can be formulated to take this into consideration to produce suitable attenuation maps [24].

There are also artifactual dense spots in the center and upper right quadrant where the two sources are located. These are most likely caused by the subtraction of the emission data from the combined emission/transmission data in the preprocessing step. The problem was most severe with large highly attenuating objects and very active emission sources. When the attenuating thickness is large, the number of photons detected from the transmission source is very low, and the combined emission/transmission counts will be nearly equal to the emission counts alone. The true transmission counts can easily be “lost” within the statistical noise of the emission counts. When the emission data is subtracted, the statistical errors are added together, resulting in a large uncertainty in the resulting transmission data. Statistical variations may result in pixels containing 0 or fewer counts, causing holes to appear in the transmission data. When converted to attenuation coefficient ray sums and backprojected the area is interpreted as being dense. Increasing the line source activity will help reduce the problem, but this will increase the radiation exposure to the patient. Increasing the line source activity will also cause problems with dead time limitations in the camera, especially if the subject being imaged doesn't cover the entire camera FOV. One possible solution is to prefilter the acquired data with a low-pass filter prior to preprocessing. This will reduce the statistical noise in the projections, and may improve the quality of the reconstructed attenuation maps.

Because of these problems associated with the attenuation map for the grid phantom, simulated attenuation maps similar to Figure 55 were generated for each phantom configuration and used with the reprojection and Chang correction methods. The attenuation map shown in Figure 55 shows the phantom (grey) with four 2x1 blocks of aluminum (white) around the central source.

FIGURE 55 Simulated attenuation map showing 4 aluminum inserts.

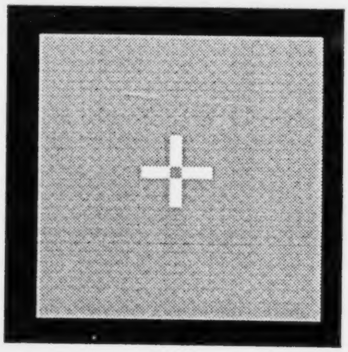

The SPECT images for each phantom configuration were corrected for attenuation using the reprojection method and Chang method with the simulated attenuation maps. Figure 56 below shows the corrected images for the reprojection method.

FIGURE 56 Reprojection corrected images.

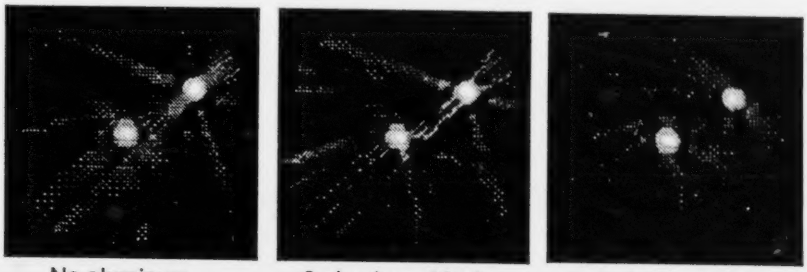

No aluminum 2 aluminum blocks 4 aluminum blocks

There is some streaking around the sources which is probably due to the discrete angular sampling during the projection process. It is interesting to note that the streaking is most visible along the direction where the attenuating thickness is greatest. This suggests that the artifacts may be related to overcorrection because of the large exponential weighting factor. Another curious thing is that there appears to be considerably more streaking in the image with no aluminum than with four aluminum blocks. The reason for this is unknown.

Line profiles through the central source of Figure 56 are shown in Figure 57.

FIGURE 57 Line profile through the central source in Figure 56.

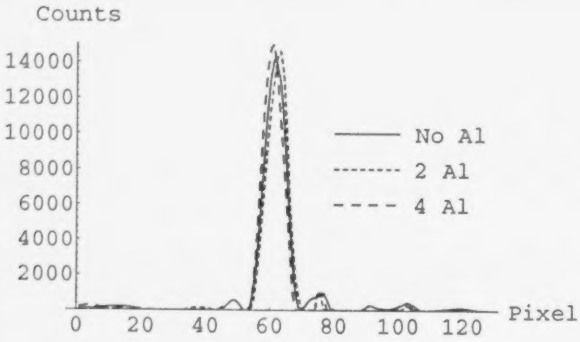

The reprojection method has kept the number of counts for each configuration fairly consistent, with a slight overcorrection for the four aluminum blocks case. In addition, the total counts has been greatly increased by about a factor of 7 over the uncorrected SPECT profiles.

Figure 58 shows the result of the Chang correction method on each of the grid phantom configurations.

FIGURE 58 Chang attenuation corrected images.

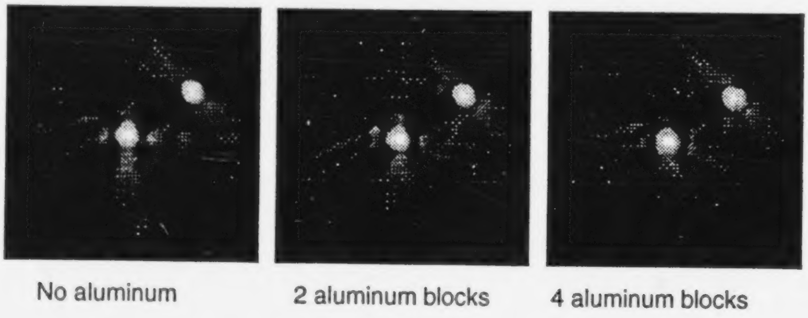
No aluminum 2 aluminum blocks 4 aluminum blocks

The background noise has been reduced slightly in the Chang corrected images compared to the original SPECT images.

Line profiles through the central sources in Figure 58 are shown below in Figure 59.

FIGURE 59 Line profiles through the central source of Figure 58.

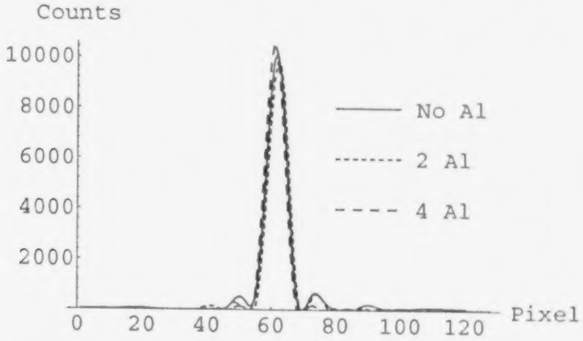

The Chang method has also kept the counts for each configuration fairly consistent, with a slight over-correction for the configuration with four aluminum blocks. The Chang method has also dramatically increased the counts by a factor of 5 over the uncorrected SPECT profiles.

Figure 60 through Figure 63 show the quantitative analysis of the grid phantom sources for zero and four blocks of aluminum around the central source. The activity concentration was 7.8 MBq/cc in the central source and 5.7 MBq/cc in the outer source and is indicated by the solid black horizontal line through each graph.

FIGURE 60 Quantitative analysis of central source with no aluminum.

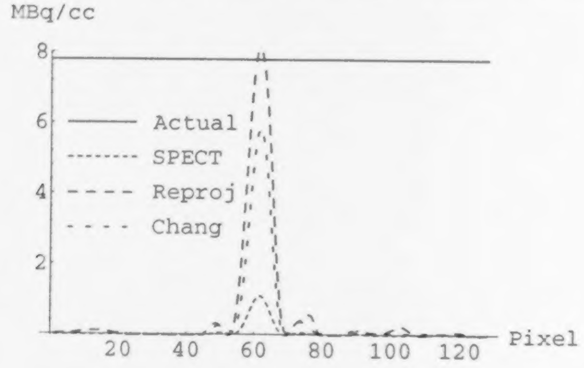

FIGURE 61 Quantitative analysis of outer source with no aluminum.

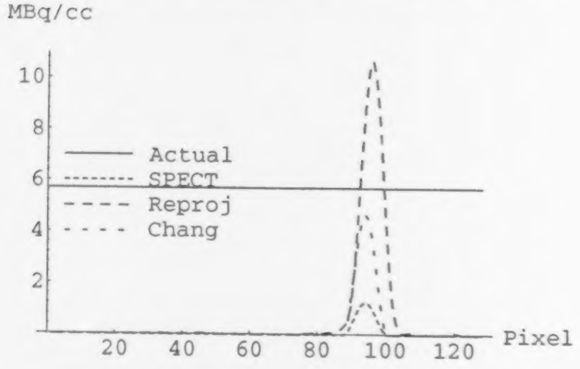

FIGURE 62 Quantitative analysis of central source with 4 aluminum blocks.

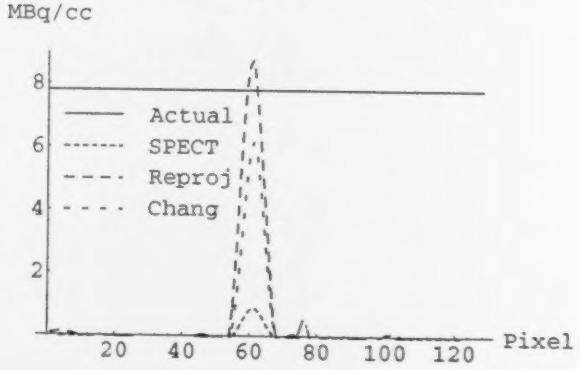

FIGURE 63 Quantitative analysis of outer source with 4 aluminum blocks.

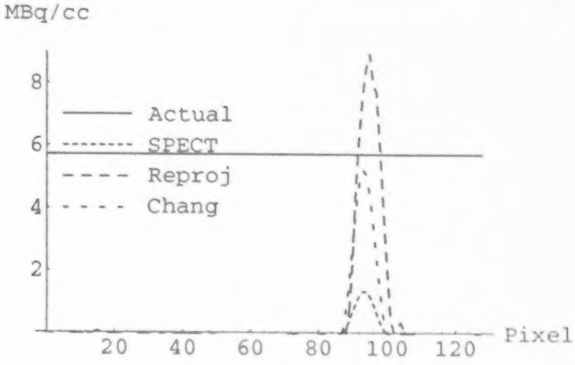

The reprojection method comes close to reproducing the actual activity concentration for the central source, but overcompensates the outer source considerably for each phantom configuration illustrated. For both the zero and four aluminum block configuration, the reprojection method comes within 15% of reproducing the actual activity concentration in the central source. For the outer source however, the reprojection method overestimates the activity concentration by almost 100% of the actual activity concentration. The Chang method comes much closer to reproducing the actual activity concentration for the outer source than it does the central source while the central sources are underestimated by as much as 25% of the actual activity concentration.

One of the reasons the outer source is being overcorrected may be due to the fact that for many of the projection angles, the outer source is projected through a large thickness of material. It therefore receives a large exponential weighting factor in those projections. At the other projection angles, the thickness of attenuating material is smaller, so the exponential weighting factor is less. When the projections are reconstructed, the most significant contribution comes from the projections where the weighting factor is greatest, while the remaining projections have a smaller contribution to the reconstruction.

CHAPTER 6

Further Work

6.1 Further Work

There remains a considerable amount of work left to be done in order to evaluate the reprojection method for accuracy.

Consideration needs to be given to optimizing the line source strength, especially for brain imaging. Since the head will not cover the entire FOV of the camera, parts of the camera will see the line source directly. If the line source is too hot, the count rate at the camera will be very high and count losses due to the dead time limitations of the camera will result. Even if the source is not very active (<200 MBq), the count rates around the subject being imaged may be high enough to cause some count losses due to dead time. These count losses can be especially detrimental for transmission imaging where the transmission counts are already low, especially for larger objects.

One modification to reduce or eliminate this problem is to add collimation in the axial direction to restrict the transmission scan field of view axially so that only the organ of interest is illuminated. Slices inferior and superior to the target organ would be shielded, reducing unnecessary patient exposure. This would be analogous to coning down the x-ray field of a regular x-ray unit to the body area of interest and would also help reduce scatter and cross-plane events by shielding the areas of the source which don't directly image the organ of interest. Although there have been few studies investigating the additional radiation exposure from the line source, it expected to be almost negligible compared to the exposure from the SPECT study. Kemp et al [30] state a value for the absorbed dose of 0.1 mGy for their collimated source. For an uncollimated source, the absorbed dose is expected to be slightly higher, however the exposure would still be small compared to the dose from a typical HM-PAO brain scan (about 3.0 mGy).

The source holder should also be modified to incorporate source collimation to reduce scatter and cross-plane events. Source collimation will dramatically improve the quality of the attenuation maps as demonstrated by Kemp et al [30] (using a line source) and Cao et al [61] (using a sheet source). The spatial resolution of the attenuation maps is determined by the resolution of the source or camera collimator, whichever has the higher resolution [61]. However, source collimation requires an increase in source activity to compensate for the photons lost due to the collimation.

Source collimation will also reduce the amount of scatter from the transmission source considerably. However, there is still a significant scatter component from the emission source which needs to be corrected for and was not considered in this work for simplicity. Scatter correction needs to be applied to remove scattered emission events from the transmission data, and to remove scatter events from the emission data in order to perform quantitative SPECT. A number of scatter correction methods can be used, including scatter fraction techniques, deconvolution methods and dual or triple energy window acquisitions.

The single line source used results in an increase in scan time, assuming the scan protocol remains the same. The single transmission source requires a 360° scan around the patient to acquire a complete set of data for the attenuation map, defeating the purpose of the triple head configuration which is supposed to reduce scan time. Cardiac SPECT studies are routinely done over 180° with modified reconstruction algorithms to compensate for the lack of data. Similar methods might be adapted to reconstructing the attenuation maps acquired over 180°.

To date, there have been few studies investigating the additional radiation exposure to patients from transmission scans. Kemp et al [30] report an absorbed dose of 0.1 mGy from a 1.1 GBq Tc-99m source over 42 minutes with their collimated line source. For uncollimated sources, this is expected to be slightly higher.

Correction for the detector response should be implemented in order to improve resolution and contrast of the reconstructed images. However, this will require a reconstruction program capable of implementing such a correction.

The projection algorithm used to perform the forward projection of the SPECT images should be modified to model the actual projection process more accurately by taking into account the detector and collimator effects and geometric response of the detector system. A more sophisticated ray tracing approach could also be considered. Rather than modelling the projection rays as a one dimensional line, a two dimensional approach could be used to model the projection rays as a two dimensional beam or strip. With such a method, the intersection area of the ray in each pixel is used to determine the appropriate weighting used to calculate the attenuation length and the projection of each image pixel.

The reprojection method requires some method of controlling the noise amplification seen with the uniform water phantom. The noise level will likely decrease with adequate source collimation, although the noise present will still be amplified and interfere with the reconstruction. Of greater concern is the overcorrection in the middle regions of the corrected image relative to the peripheral regions. This overcorrection was thought to be due to the large exponential weighting of pixels located far away from the detector. This could cause problems when applied to brain images which are somewhat close to a uniformly emitting activity distribution.

CHAPTER 7 Conclusion

7.1 Conclusion

The purpose of this project was to investigate a new method of performing attenuation correction using an external line source to obtain a non-uniform attenuation map of the body. The reconstructed SPECT images were used to estimate the contribution of each pixel (voxel) to the projection data and weighted by $exp\left(\int\mu\,(x, y)\,dy\right)$ to correct for attenuation.

The use of an external line source is a proven method of obtaining an attenuation map of the body for attenuation correction. The line source holder developed for this project is easy to build and requires only minimal modification to the SPECT gantry. One of the limitations to the line source configuration used was that the minimum head orbit radius was about 15 cm measured from the center of rotation to the surface of the head. This was the smallest head orbit radius possible without experiencing severe truncation of the line source from heads 2 and 3. Typical brain SPECT studies are normally performed with a head radius of between 13 - 14 cm to optimize sensitivity and resolution.

The attenuation maps produced by the line source are of suitable quality to be used in attenuation correction. High contrast resolution of the transmission maps was found to be better than 6.4 mm in a scatter free environment determined from a transmission scan of the Jaszczak phantom. With the presence of scatter, the resolution is expected to decrease somewhat. The uniformity properties as demonstrated by the attenuation map of the uniform water phantom appear to be adequate, although the attenuation coefficients are slightly underestimated due to scattered events from both the transmission and emission sources.

Experiments with the uniform water phantom show that the noise properties of the algorithm are unacceptable at this point for implementation. The algorithm also appears to be unable to handle a uniform activity distribution. Central regions of the phantom are overcorrected compared to the edges of the phantom. Further enhancements and modifications to the line source, acquisition protocols and processing methods may improve the corrected images.

In all phantom studies, the reprojection algorithm significantly increased the counts in the corrected images compared to the original SPECT counts, with background counts decreased relative to the corrected SPECT counts. Count levels were also increased relative to the counts in the images corrected with the Chang algorithm. The problems with the simple quantitative analysis performed (overcorrected for the uniform water phantom, about right for the grid phantom, and under-corrected for the brain phantom) could be due to a flaw in the analysis method. The analysis assumes that there is some direct linear relationship between the activity concentration in the object and the pixel values reconstructed in the SPECT images. Whether this linear relationship is preserved after the reprojection method is applied still needs to be determined. The assumption that the reconstructed SPECT images can be used to estimate the contributions of the individual pixels to the projections must also be investigated further.

The reprojection algorithm is a simple approach to the attenuation problem and is easily implemented, requiring only two additional processing steps. The line source was designed to be practical and simple requiring little operator setup. With further investigation, the reprojection algorithm developed here may lead to a useful and practical attenuation correction method.

CHAPTER 8

Appendix A: Program listings

8.1 Transmission scan conversion program

A C program was written in order to convert the transmission study into attenuation coefficient ray sums which could be reconstructed into an attenuation map. The following two code fragments show how the emission data was subtracted from the combined emission/transmission data, and the conversion to attenuation coefficients.

8.1.1 Transmission/emission data subtraction

The code fragment below is responsible for removing the emission data from the combined transmission/emission data. The emission data from heads 2 and 3 are summed together to improve the count statistics, while the average of the data from heads 2 and 3 are subtracted from the transmission/emission data from head 1. Any pixels which have a value less than 0 are set to 1.

```
/*
 * Add the data from heads 2 and 3
 * Subtract emission data from transmission data and replace
 * negative pixels with 1
 */
for (i=0;i<pixels;i++) {
  emission2[i] = ((emission2[i] + emission3[i]) -
ABS(emission2[i] - emission3[i]));
  trndata[i] -= (emission2[i]>>1);
 if (trndata[i] < 0) trndata[i] = 1;
}
```

8.1.2 Transmission to μ conversion

This code fragment converts the transmission data to attenuation coefficients in cm^{-1} using Equation 14. The variable `refdata[]` is used to store the reference scan of the line source. Since the SPECT data is stored in 16 bit integers (short int), the resulting attenuation coefficients are scaled by a factor of 100 to convert them to integers.

```
/*
 * Compute SUM(mu*dx) = C*ln(Io/I) where C is a scaling factor
 * which lets me store the ray sums as short ints
 * C = 100
 */
for (n=0;n<nprj;n++) {          /* cycle through each slice */
  for (i=0;i<piximg;i++) {     /* calc attenuation ray sum */
    if (trndata[i+n*piximg] > 0) { /* check divide by zero */
      attnsum[i+n*piximg] = log((double )refdata[i]/(double
)trndata[i+ n*piximg])*scale;
    }
  }
}
```

8.2 Fan beam projection algorithm

8.2.1 Ray tracing algorithm

The subroutine below shows an implementation of the ray tracing algorithm developed by Siddon. The subroutine calculates the pixel intersection lengths for a set of fan beam rays through the image matrix. The intersection lengths are calculated once and stored in memory in the variable `alen[]`. The values in `amid[]` are used to calculate the array indices of the pixel being intersected.

```
void calcFanRays()
{
/*
 * Calculate intersection parameters for fan beam geometry
 * using Siddon's algorithm
 */
    register int k, l, m;
    int dim2;                /* matrix dimension/2 */
    int nx, ny;              /* matrix x,y dimensions */
    int px;                  /* projection pixels */
    int focalLength;         /* fan beam focal length (mm) */
    int headRadius;          /* head radius (mm) */
    float imgPixSize;        /* image pixel size (mm) */
    float projPixSize;       /* projection pixel size (mm) */
    float detPlane;          /* detector plane offset from origin */
    float rise, run;         /* proj ray rise/run */
    float a, b;              /* temp storage */
    float amin, amax;        /* max/min intersection params */
    float pnx;               /* pos of edge of img matrix */
    float *alpha;            /* intersection values */
    float raylen;            /* projection ray length (cm) */
    struct point alphax, alphay;
    struct point p1,p2;      /* start/end point of ray */
    struct coord i, j;       /* range of intersected pixels */

    nx = spectIIB.rmx;
    ny = spectIIB.rmy;
    px = spectIIB.amx;       /* acq matrix pixels */
    dim2 = nx/2;
    imgPixSize = atof(spectIIB.rpx);
```

```
  projPixSize = atof(spectIIB.apx);
  pnx = nx*imgPixSize;
  focalLength = 500;
  headRadius = spectIIB.orm[0]*.1;
  detPlane = dim2*imgPixSize + headRadius;
  p1.x = dim2*imgPixSize;         /* focal point x */
  p1.y = detPlane - focalLength; /* focal point y */
  p2.x = -dim2*(projPixSize-imgPixSize)+projPixSize/2; /* proj pix
x */
  p2.y = detPlane;                /* proj pix y */
  rise = p2.y - p1.y;

  amid = (float **)malloc(nx*sizeof(float *));
  if (amid == NULL) {
    fprintf(stderr, "   amid initialization failed\n");
    exit(-1);
  }
  alen = (float **)malloc(nx*sizeof(float *));
  if (alen == NULL) {
    fprintf(stderr, "    alen initialization failed\n");
    exit(-1);
  }

  /* Number of intersection points for each ray */
  numalpha = (int *)malloc(nx*sizeof(int));
  if (numalpha == NULL) {
    fprintf(stderr, "    ray parameter initialization failed\n");
    exit(-1);
  }
  for (k=0;k<nx;k++) numalpha[k] = 0;

  /* Calculate intersection parameters */
  for (k=0;k<px;k++) {             /* for each proj pixel */
    run = p2.x - p1.x;
    /* Calc projection ray length in cm */
    raylen = sqrt(sqr(rise) + sqr(run))*.1;
    /* Calc max/min intersection parameter */
    alphax.x = -p1.x/run;
    alphax.y = (pnx - p1.x)/run;
    alphay.x = -p1.y/rise;
    alphay.y = (pnx - p1.y)/rise;
    a = min(alphax.x, alphax.y);
    b = min(alphay.x, alphay.y);
    amin = max(a, b);
    a = max(alphax.x, alphax.y);
    b = max(alphay.x, alphay.y);
    amax = min(a, b);
    /* Calc range of intersected pixel indices */
    if (run > 0) {
      i.x = nx - (int )((pnx - amin*run - p1.x)/imgPixSize);
      i.y = (int )((p1.x + amax*run)/imgPixSize);
    }
    else {
      i.x = nx - (int )((pnx - amax*run - p1.x)/imgPixSize);
      i.y = (int )((p1.x + amin*run)/imgPixSize);
    }
    j.x = ny - (int )((pnx - amin*rise - p1.y)/imgPixSize);
    j.y = (int )((p1.y + amax*rise)/imgPixSize);
    /* Number of intersections */
    numalpha[k] = ABS(i.y - i.x) + ABS(j.y - j.x) + 1;
    alpha = (float *)malloc(numalpha[k]*sizeof(float));
    amid[k] = (float *)malloc(numalpha[k]*sizeof(float));
    alen[k] = (float *)malloc(numalpha[k]*sizeof(float));
    /* Calc intersection parameters */
    l = 0;
    for (m=i.x;m<i.y;m++) {
      alpha[l] = (m*imgPixSize - p1.x)/run; l++;
    }
    for (m=j.x;m<j.y;m++) {
      alpha[l] = (m*imgPixSize - p1.y)/rise; l++;
    }
    alpha[l] = amax; l++;
    /* Sort intersection parameters */
    qsort(&alpha[0], numalpha[k], sizeof(float), fcmp);
    for (l=1;l<numalpha[k];l++) {
      amid[k][l] = (alpha[l] + alpha[l-1])*.5;
      alen[k][l] = (alpha[l] - alpha[l-1])*raylen;
    }
    numalpha[k]--;
    p2.x += projPixSize;
    free(alpha);
  }

  return;
}
```

8.2.2 Fan beam projection routine

The subroutine below uses the pixel intersection lengths calculated in the subroutine described above. At each projection angle, the SPECT and attenuation map arrays are rotated using a floating point rotation algorithm and projected.

```
void project()
{
/*
 * Project the SPECT data using a fan beam geometry.
 * Projection data are calculated using trapezoidal rule to evaluate
 * the line integral along the projection ray.
 * Should use a more sophisticated integration method
 *
 * Calling arguments -
 *
 */

    register int i, j, k, sl, p;        /* loop index variables */
    register int a, b;           /* indices of intersected pixel */
    register int idx;            /* intersected pixel array index */
    int nx, ny;                         /* image array dimensions */
    int dim2;                           /* nx/2 */
    int piximg;                         /* # pixels/image */
    int sliceoffset;             /* y offset from top of each proj */
    int sln;                            /* number of slices */
    float angle;                 /* rotation angle in radians */
    float dtheta;                       /* rotation angle increment */
    float pixsize;                      /* pixel size (mm) */
    float *datarot;                     /* rotated data value */
    float olddata;                      /* previous data value */
    float *murot;                       /* rotated mu value */
    float oldmu;                        /* previous mu value */
    float rise, run;             /* rise/run of proj ray (mm) */
    float projPixSize;           /* projection pixel size (mm) */
    float len;
    double attenl;                      /* attenuation length */
    double sum;                         /* proj ray sum */
    struct point p1, p2;      /* start/end points of proj ray (mm) */

    /*
     * Set up a few required values
     */
    nx = spectIIB.rmx;
    ny = spectIIB.rmy;
    sln = (int )spectIIB.sln;
    pixsize = (float )atof(spectIIB.rpx);
    dim2 = nx/2;
    projPixSize = (float )atof(spectIIB.apx);
    piximg = nx*ny;
    sliceoffset = (ny - sln)/2;
    attenl = 0.0;
    angle = 0.0;
    dtheta = M_PI/60;            /* 3 degree rotation increment */
```

```
p1.x = dim2*pixsize;        /* focal point x */
p1.y = dim2*pixsize+spectIIB.orm[0]*.1-500; /* focal pt y */
p2.y = dim2*pixsize + spectIIB.orm[0]*.1; /* proj plane */
rise = 500;

/*
 * Allocate space to hold the rotated slices
 */
datarot = (float *)malloc(piximg*sln*sizeof(float));
if (datarot == NULL) {
  fprintf(stderr, "datarot initialization failed\n");
  exit(-1);
}
murot = (float *)malloc(piximg*sln*sizeof(float));
if (murot == NULL) {
  fprintf(stderr, "murot initialization failed\n");
  exit(-1);
}

/*
 * Convert attn map to attenuation coefficients
 */
for (i=0;i<piximg*sln;i++) {
  /*  convert to attn coeffs */
  attn[i] = .000290529*attn[i] - .00148865;
}
for (i=0;i<piximg*sln;i++) {
  if (attn[i]<0.0) attn[i] = 0.0;
}

for (k=0;k<120;k++) {            /* for each rotation angle */
  /* Rotate spect and attn data by angle radians */
  frotate(spect, datarot, nx, ny, sln, angle, NULL);
  frotate(attn, murot, nx, ny, sln, angle, NULL);
  for (sl=0;sl<sln;sl++) {         /* for each slice */
    /* location of current pixel in projection matrix */
    p = k*piximg + (sl + sliceoffset)*nx + nx - 1;
    /* reset proj pix location */
    p2.x = -dim2*(projPixSize - pixsize) + projPixSize/2;
    for (j=0;j<nx;j++) {    /* for each projection pixel */
      attenl = 0.0;            /* Reset attenl */
      sum = 0.0;               /* Reset proj sum */
      olddata = 0.0;
      oldmu = 0.0;
      run = p2.x - p1.x;
      i = numalpha[j] - 1;
      do {               /* for each intersected pixel */
        /* calc index of intersected pixel */
```

```
           a = (p1.x + amid[j][i]*run)/pixsize;
           b = (p1.y + amid[j][i]*rise)/pixsize;
           idx = sl*piximg + b*nx + a;
           /*
           * Integrate over SPECT distribution and attn map
           * using trapezoidal rule
           * (f(a) + f(b))/2 + SUM(f(xi))
           *
           */
           sum += (datarot[idx]+olddata)*0.5*exp(attenl)*
alen[j][i];
           attenl += alen[j][i]*(murot[idx] + oldmu)*0.5;
           olddata = datarot[idx];
           oldmu = murot[idx];
           i--;
         } while (i);
         proj[p] = (short )(sum/120);
         p--;                   /* Next projection pixel */
         p2.x += projPixSize;
       }
     }
     angle += dtheta;                /* Next rotation angle */
   }

   free(datarot);
   free(murot);

   return;
}
```

8.3 Non-uniform Chang algorithm

This subroutine calculates the Chang correction matrix, C(x,y) given in Equation 11, substituting the attenuation map stored in the array `attn[]` for μ(x,y) and using the intersection lengths calculated using a variation of the subroutine in 8.2.1. The pixel intersection parameters (`alpha[][]`) are calculated in advance for a series of M rays originating from the origin. For each pixel in the correction matrix, the origin of the rays is shifted within the image matrix and the number of intersection parameters is calculated. The intersection lengths are then calculated from `alpha[][]` for the number of pixels intersected and used to compute `cm[]`.

```
void calcCorrMatrix()
{
/*
 * Calculates the elements of the correction matrix which will be
used to
 * implement a 1st order Chang attenuation correction.
 * This routine loops through each pixel, and for each ray uses
 * the predetermined intersection parameters to calculate the
intersected
 * length within the pixel.  For each pixel, 120 rays are
calculated.
 * The loop is started at 2 degrees and incremented by 3 degrees to
 * avoid dealing with 0, 45, 90, 135, 180, 225, 270 and 315 degrees
 * which could cause potential problems with the algorithm as it is
 * currently implemented.
 *
 * Calling arguments - None
 *
 */

    register int i, k, l, m;
    int pixnum;                      /* total number of pixels */
    int piximg;                      /* number of pixels/image */
    int dim;                         /* dimension of image array */
    int n;                         /* number of intersected pixels */
    int slice;
    int x1, x2, y1, y2;
    float pixsize;                   /* pixel size */
    float pnx;
    float rise, run;
    float attenl;
    float raylength;                 /* ray length */
    float alphamax, amid;
    float sum;
    float len;
    float a, b;
    float a1, a2;
    struct point
    {
      double x, y;
    } p1;

    pixsize = atof(attnIIB.rpx)*.1; /* pixel size in cm */
```

Non-uniform Chang algorithm

```
dim = attnIIB.rmx;
piximg = sqr(dim);
pixnum = piximg*attnIIB.sln;
raylength = M_SQRT2*dim*pixsize;    /* ray length in cm */
pnx = dim*pixsize;

/*
 * Allocate space for correction matrix and init to 1.0
 */
cm = (float *)malloc(pixnum*sizeof(float));
for (l = 0; l < pixnum; l++) cm[l] = 1.0;

/*
 * Go through the image matrix and calc the correction matrix
 */
for (l = 0; l < pixnum; l++) {
  slice = l/piximg;
  p1.x = ((l % piximg) % dim)*pixsize + pixsize*.5;
  p1.y = ((l % piximg) / dim)*pixsize + pixsize*.5;
  sum = 0.0;          /* Reset sum of attenuation factors */
  if (attn[l] > 0) {
  for (m = 0; m < 120; m++) {
    attenl = 0.0;          /* reset attenuation length */
    rise = raylength*st[m];
    run = raylength*ct[m];
    /* Calculate max intersection parameter */
    a = max((-p1.x)/run, (pnx - p1.x)/run);
    b = max((-p1.y)/rise, (pnx - p1.y)/rise);
    alphamax = min(a, b);
    if (alphamax > 1.0) alphamax = 1.0;
    /*
    * Calculate the number of intersection parameters
    */
    if (run > 0) {
      x1 = dim - (int )((pnx - p1.x)/pixsize);
      x2 = (int )((p1.x + alphamax*run)/pixsize) + 1;
    }
    else {
      x1 = dim - (int )((pnx - alphamax*run - p1.x)/pixsize);
      x2 = (int )(p1.x/pixsize) + 1;
    }
    if (rise > 0) {
      y1 = dim - (int )((pnx - p1.y)/pixsize);
      y2 = (int )((p1.y + alphamax*rise)/pixsize) + 1;
    }
    else {
      y1 = dim - (int )((pnx - alphamax*rise - p1.y)/pixsize);
      y2 = (int )((p1.y + alphamax*rise)/pixsize) + 1;
      }
      n = ABS(x2 - x1) + ABS(y2 - y1);
      for (k = 1; k < n-1; k++) {
        a1 = alpha[m][k];
        a2 = alpha[m][k-1];
        /*
         * Calculate the indices of the interesected pixel
         */
        amid = (a1 + a2)/2;
        i = (int )((p1.x+amid*run)/pixsize)+(int )((p1.y +
amid*rise)/pixsize)*dim;
        len = raylength*ABS(a1 - a2);
        /*
        * Now calculate the attenuation length of the ray
        */
        attenl += attn[slice*piximg + i]*len;
      }
      sum += exp(-attenl);
    }
  cm[l] = 120/sum;
  }
}
```

CHAPTER 9

Bibliography

1. Jaszczak RJ, Coleman RE. "Single Photon Emission Computed Tomography (SPECT): Principles and Instrumentation", *Invest Radiol* ***20***:895-910 1985

2. King MA, Schwinger RB, Doherty PW, Penney BC, "Two-dimensional filtering of SPECT images using the Metz and Wiener filters", *J Nucl Med* **25**:1234-1240 1984

3. Miller MI, Snyder DL, Miller TR, "Maximum likelihood reconstruction for Single Photon Emission Computed Tomography", *IEEE Trans Nucl Sci* ***32***:769-778 1985

4. Munley MT, Floyd Jr, CE, Bowsher JE, Coleman RE, "An artificial neural network approach to quantitative single photon emission computed tomographic reconstruction with collimator, attenuation and scatter compensation", *Med Phys* **21**:1889-1899 1994

5. Kemp BJ, Prato FS, Dean GW, Nicholson L, Reese L., "Correction for attenuation in technetium-99m-HMPAO SPECT brain imaging", *J Nucl Med* ***33***:1875-1880 1992

6. Zhang JJ, Park CH, Kim SM, Intenzo C, Reyes P, "The attenuation effect in brain SPECT", *Clin Nucl Med*, **18**:583-586 1993

7. Malko JA, Van Heertum RL, Gullberg GT, Kowalsky WP, "SPECT liver imaging using an iterative attenuation correction algorithm and an external flood source", *J Nucl Med* ***27***:701-705 1986

8. Tsui BMW, Zhao X, Frey EC, McCartney WH. "Quantitative single photon emission computed tomography: Basics and clinical considerations", *Semin Nucl Med* ***24***:38-65 1994

9. Manglos SH, Thomas FD, Gagne GM, Hellwig BJ, "Phantom study of breast tissue attenuation in myocardial imaging", *J Nucl Med* ***34***:992-996 1993

10. Tretiak O, Metz C, "The exponential radon transform", *SIAM J Appl Math* ***39***:341-354 1980

11. Gullberg GT, Huesman RH, Malko JA, Pelc NJ, Budinger TF, "An attenuated projector-backprojector for iterative SPECT reconstruction", *Phys Med Biol* ***30***:799-816 1985

12. Chang LT, "A method for attenuation correction in radionuclide computed tomography", *IEEE Trans Nucl Sci* ***25***:538-539 1978

13. Tanaka E, "Quantitative image reconstruction with weighted backprojection for Single Photon Emission Computed Tomography", *J Comput Assist Tomog* ***7***:692-700 1983

14. Manglos SH, Jaszczak RJ, Floyd CE, "Weighted backprojection implemented with a non-uniform attenuation map for improved SPECT quantitation", *IEEE Trans Nucl Sci* ***35***:625-628 1988

15. Chornoboy ES, Chen CJ, Miller MI, Miller TR, Snyder DL, "An evaluation of maximum likelihood reconstruction for SPECT", *IEEE Trans Med Imag* ***9***:99-110 1990

16. Fleming JS, "A technique for using CT images in attenuation correction and quantification in SPECT", *Nucl Med Commun* **10**:83-97 1989

17. Ficaro EP, Fessler JA, Rogers WL, Schwaiger M, "Comparison of americium-241 and technetium-99m as transmission sources for attenuation correction of thallium-201 SPECT imaging of the heart", *J Nucl Med* ***35***:652-663 1994

18. Welch A, Gullberg GT, Christian PE, Datz FL, "A comparison of Gd/Tc versus Tc/Tl simultaneous transmission and emission imaging using both single and triple detector fan beam SPECT systems", *IEEE Trans Nucl Sci* **41**:2779-2786 1994

19. Bailey DL, Hutton BF, Walker PJ, "Improved SPECT using simultaneous emission and transmission tomography", *J Nucl Med* ***28***:844-851 1987

20. Tan P, Bailey DL, Meikle SR, Eberl S, Fulton RR, Hutton BF, "A scanning line source for simultaneous emission and transmission measurements in SPECT", *J Nucl Med* **34**:1752-1760 1993

21. Larsson SA, Kimiaei S, Ribbe T, "Simultaneous SPECT and CT with shutter controlled radionuclide sources and parallel collimator geometry", *IEEE Trans Nucl Sci* **40**:1117-1122 1993

22. Manglos SH, Bassano DA, Duxbury CE, Capone RB, "Attenuation maps for SPECT determined using cone beam transmission computed tomography", *IEEE Trans Nucl Sci* ***37***:600-608 1990

23. Datz FL, Gullberg GT, Zeng GL, Tung CH, Christian PE, "Application of convergent beam collimation and simultaneous transmission emission tomography to cardiac single photon emission computed tomography", *Semin Nucl Med* **24**:17-37 1994

24. Tung CH, Gullberg GT , Zeng GL, Christian PE, Datz EL, Morgan HT, "Non-uniform attenuation correction using simultaneous transmission and emission converging tomography", *IEEE Trans Nucl Sci* ***39***:1134-1143 1992

25. Jain AK. Image Reconstruction from Projections. In: Fundamentals of Image Processing, Prentice Hall, Inc 431-471 1989

26. Hubbell HJ, "Photon cross sections, attenuation coefficients and energy absorption coefficients from 10 keV to 100 GeV", National Bureau of Standards NSRDS-NBS-29 1969

27. Siddon RL, "Fast calculation of the exact radiological path for a three dimensional CT array", *Med Phys* ***12***:252-255 1985

28. Taylor JR, An introduction to error analysis, University Science Books 1992

29. Zeng GL, Gullberg GT, "Frequency domain implementation of the three-dimensional geometric response correction in SPECT imaging", *IEEE Trans Nucl Sci* **33**:1444-1453 1992

30. Kemp BJ, Prato FS, Nicholson RL, Reese L, "Transmission computed tomography imaging of the head with a SPECT system and a collimated line source", *J Nucl Med* **36**:328-335 1995

31. Manglos SH, Thomas FD, Hellwig BJ, "The effects of non-uniform attenuation compensation on myocardial SPECT defect analysis", *Phys Med Biol* ***38***:897-907 1993

32. Gullberg GT, Malko JA et al, Application of Attenuation Correction to Clinical Data, GE Publication 5408

33. Manglos SH, Jaszczak RJ, Floyd CE, Hahn LJ, Greer KL, Coleman RE, "Nonisotropic attenuation in SPECT: Phantom tests of quantitative effects and compensation techniques", *J Nucl Med* ***28***:1584-1591 1987

34. Bourguignon MH, Berrah H, Berdriem B, Riddell C, Valette H, Wartski M, De Dreuille O, Jouve B, Syrota A, "Correction of attenuation in SPECT with an attenuation coefficient map: A new method", *J Nucl Biol Med* ***37***:26-32 1993

35. Almquist H, Palmer J, Ljungberg M, Wollmer P, Strand SE, Jonson B, "Quantitative SPECT by attenuation correction of the projection set using transmission data: Evaluation of a method", *Eur J Nucl Med* ***16***:587-594 1989

36. Manglos SH, Bassano DA, Thomas FD, "Cone-beam transmission computed tomography for nonuniform attenuation compensation of SPECT images", *J Nucl Med* ***32***:1813-1820 1991

37. Frey EC, Tsui BMW, Perry JR, "Simultaneous acquisition of emission and transmission data for improved thallium-201 cardiac SPECT imaging using a technetium-99m transmission source. *J Nucl Med* ***33***:2238-2245 1992;

38. Tsui BMW, Gullberg GT, Edgerton ER, Ballard JG, Perry JR, McCartney WH, Berg J, "Correction of nonuniform attenuation in cardiac SPECT imaging", *J Nucl Med* ***30***:497-507 1989

39. Jaszczak RJ, Gilland DR, Hanson MW, Jang S, Greer KL, Coleman RE, "Fast transmission CT for determining attenuation maps using a collimated line source, rotatable air-copper-lead attenuators and fan-beam collimation", *J Nucl Med* ***34***:1577-1586 1993

40. Galt JR, Cullom SJ, Garcia EV, "SPECT quantification: A simplified method of attenuation and scatter correction for cardiac imaging", *J Nucl Med* **33**:2232-2237 1992

41. Tanaka E, "Convolutional image reconstruction for quantitative Single Photon Emisison Computed Tomography", *Phys Med Biol* **29**:1489-1500 1984

42. Shepp LA, Vardi Y, "Maximum likelihood reconstruction for emission tomography", *IEEE Trans Med Imag* ***1***:113-122 1982

43. Miller TR, Wallis JW, "Clinically important characteristics of maximum likelihood reconstruction", *J Nucl Med* ***33***:1678-1684 1992

44. Brooks RA, Di Chiro G, "Theory of image reconstruction in computed tomography", *Radiology* ***117***:561-572 1975

45. Gullberg GT, Zeng GL, Datz FL, Christian PE, Tung CH, Morgan HT, "Review of convergent beam tomography in Single Photon Emission Computed Tomography", *Phys Med Biol* ***37***:507-534 1992

46. Kak AC, Slaney M, "Algorithms for reconstruction with nondiffracting sources", In: Principles of Computerized Tomographic Imaging, pg 60-143 IEEE Press 1987

47. Lange K, Carson R, "EM reconstruction algorithms for emission and transmission tomography", *J Comput Assist Tomog* ***8***:306-316 1984

48. Ljungberg M, Strand SE, "Attenuation correction in SPECT based on transmission studies and Monte Carlo simulations of build-up functions", *J Nucl Med* ***31***:493-500 1990

49. Manglos SH, Jaszczak RJ, Floyd CE, Hahn LJ, Greer KL, Coleman RE, "A quantitative comparison of attenuation-weighted backprojection with multiplicative and iterative postprocessing attenuation compensation in SPECT", *IEEE Trans Med Imag* **7**:127-134 1988

50. Maze A, Cloirec JL, Collorec R, Bizais Y, Briandet P, Bourguet P, "Iterative Reconstruction Methods for Nonuniform Attenuation Distribution in SPECT", *J Nucl Med* ***34***:1204-1209 1993

51. Murase K, Itoh H, Mogami H, Ishine M, Kawamura M, Iio A, Hamamoto K, "A comparative study of attenuation correction algorithms in Single Photon Emission Computed Tomography (SPECT)", *Eur J Nucl Med* ***13***:55-62 1987

52. Rowell NP, Glaholm J, Flower MA, Cronin B, McCready VR, "Anatomically derived attenuation coefficients for use in quantitative Single Photon Emission Tomography studies of the thorax", *Eur J Nucl Med* ***19***:36-40 1992

53. Walters TE, Simon W, Chesler DA, Correia JA, "Attenuation correction in gamma emission computed tomography", *J Comput Assist Tomog* ***5***:89-94 1981

54. Ye J, Liang Z, Harrington DP, "Quantitative reconstruction for myocardial perfusion SPECT: An efficient approach by depth-dependent deconvolution and matrix rotation", *Phys Med Biol* **39**:1263-1279 1994

55. Zeng GL, Hsieh YL, Gullberg GT, "A rotating and warping projector/backprojector for fan-beam and cone-beam iterative algorithms", *IEEE Trans Nucl Sci* **41**:2807-2811 1994

56. Bushberg JT, Seibert JA, Leidholdt Jr EM, Boone JM, "Interaction of radiation with matter", In: The Essential Physics of Medical Imaging, Williams & Wilkins, 1994

57. Johns HE, Cunningham JR, Table 5-5 In: The Physics of Radiology, 4th ed., pg 163, Charles C Thomas Publ, 1983

58. Liang Z, "Compensation for attenuation, scatter, and detector response in SPECT reconstruction via iterative FBP methods", *Med Phys* **20**:1097-1106 1993

59. Eisner RL, Nowak DJ, Pettigrew R, Fajman W, "Fundamentals of 180° acquisition and reconstruction in SPECT imaging", *J Nucl Med* **27**:1717-1728 1986

60. Go RT, MacIntyre WJ, Houser TS, Pantoja M, O'Donnell JK, Feiglin DH, Sufka BJ, Underwood DA, Meaney TF, "Clinical evaluation of 360° and 180 ° data sampling techniques for transaxial SPECT tallium-201 myocardial perfusion imaging", *J Nucl Med* **26**:695-706 1985

61. Cao ZJ, Tsui BMW, "Performance characteristics of transmission imaging using a uniform sheet source with parallel hole collimation", *Med Phys* **19**:1205-1212 1992

62. Buvat I, Benali H, Todd-Pokropek A, Di Paola R, "Scatter correction in scintigraphy: the state of the art", *Eur J Nucl Med* **21**:675-694 1994

63. Sorensen JA, Phelps ME, Physics in Nuclear Medicine, 2nd ed., W.B. Saunders Co., 1987

64. Picker International, Odyssey Operator's Guide, 1993